

## RESEARCH ARTICLE

10.1002/2017JA024971

## Key Points:

- The axial magnetic flux and helicity of the magnetic cloud decreased with the heliocentric distance, but the twist increased
- The “pancaking” effect and “erosion” effect may jointly cause the variations of the flux, helicity, and twist
- The erosion effect together with the variations implies that the magnetic cloud probably carried a high-twist core

## Correspondence to:

Y. Wang,  
ymwang@ustc.edu.cn

## Citation:

Wang, Y., Shen, C., Liu, R., Liu, J., Guo, J., Li, X., et al. (2018). Understanding the twist distribution inside magnetic flux ropes by anatomizing an interplanetary magnetic cloud. *Journal of Geophysical Research: Space Physics*, 123, 3238–3261. <https://doi.org/10.1002/2017JA024971>

Received 4 NOV 2017

Accepted 25 FEB 2018

Accepted article online 5 MAR 2018

Published online 3 MAY 2018

## Understanding the Twist Distribution Inside Magnetic Flux Ropes by Anatomizing an Interplanetary Magnetic Cloud

Yuming Wang<sup>1,2</sup> , Chenglong Shen<sup>1,2</sup>, Rui Liu<sup>1,3</sup> , Jiajia Liu<sup>4</sup>, Jingnan Guo<sup>5</sup> , Xiaolei Li<sup>1,3</sup>, Mengjiao Xu<sup>1,3</sup>, Qiang Hu<sup>6</sup> , and Tielong Zhang<sup>1,3,7</sup> 

<sup>1</sup>CAS Key Laboratory of Geospace Environment, School of Earth and Space Sciences, University of Science and Technology of China, Hefei, China, <sup>2</sup>Synergetic Innovation Center of Quantum Information and Quantum Physics, University of Science and Technology of China, Hefei, China, <sup>3</sup>Collaborative Innovation Center of Astronautical Science and Technology, Hefei, China, <sup>4</sup>Solar Physics and Space Plasma Research Center, School of Mathematics and Statistics, University of Sheffield, Sheffield, UK, <sup>5</sup>Institute of Experimental and Applied Physics, University of Kiel, Kiel, Germany, <sup>6</sup>Department of Space Science and CSPAR, The University of Alabama in Huntsville, Huntsville, AL, USA, <sup>7</sup>Space Research Institute, Austrian Academy of Sciences, Graz, Austria

**Abstract** Magnetic flux rope (MFR) is the core structure of the greatest eruptions, that is, the coronal mass ejections (CMEs), on the Sun, and magnetic clouds are posteruption MFRs in interplanetary space. There is a strong debate about whether or not a MFR exists prior to a CME and how the MFR forms/grows through magnetic reconnection during the eruption. Here we report a rare event, in which a magnetic cloud was observed sequentially by four spacecraft near Mercury, Venus, Earth, and Mars, respectively. With the aids of a uniform-twist flux rope model and a newly developed method that can recover a shock-compressed structure, we find that the axial magnetic flux and helicity of the magnetic cloud decreased when it propagated outward but the twist increased. Our analysis suggests that the “pancaking” effect and “erosion” effect may jointly cause such variations. The significance of the pancaking effect is difficult to be estimated, but the signature of the erosion can be found as the imbalance of the azimuthal flux of the cloud. The latter implies that the magnetic cloud was eroded significantly leaving its inner core exposed to the solar wind at far distance. The increase of the twist together with the presence of the erosion effect suggests that the posteruption MFR may have a high-twist core enveloped by a less-twisted outer shell. These results pose a great challenge to the current understanding on the solar eruptions as well as the formation and instability of MFRs.

**Plain Language Summary** Magnetic Flux rope (MFR) is a fundamental structure in the universe filled with plasmas and related to various eruptive phenomena, for example, mass ejections and jets. How the magnetic twist distributes in a MFR is key information in understanding many puzzles: for example, (1) why a very long (thousands of light years long) and high-twist astrophysical jet can exist, (2) whether or not a seed MFR exists prior to coronal mass ejections, which is a long debate in the solar physics, and (3) when a MFR gets kink unstable. Here we try to address these puzzles by presenting a rare observed MFR, namely, magnetic cloud, in interplanetary space. Four spacecraft near Mercury, Venus, Earth, and Mars, respectively, observed the magnetic cloud sequentially in time and space. By analyzing the in situ measurements of the magnetic cloud, we find that the axial flux and helicity decreased with the heliocentric distance but the twist increased. The “pancaking” effect and “erosion” effect may jointly cause such variations. The erosion effect suggests that the magnetic cloud might consist of a strong-twist core and a less-twisted outer shell, posing a great challenge to the current understanding on the solar eruptions as well as the formation and instability of MFRs.

## 1. Introduction

Magnetic flux rope (MFR) is a fundamental plasma structure in the universe and tightly related to various eruptive phenomena due to nonpotential field therein. It could appear in magnetic reconnection regions manifesting as magnetic islands (e.g., Daughton et al., 2011), in the corona and heliosphere known as coronal mass ejections (CMEs) and magnetic clouds (e.g., Burlaga et al., 1981; Vourlidas et al., 2013; Zhang et al., 2012), and in astrophysical jets with the scale up to thousands of light years (e.g., Marscher et al., 2008;

Owen et al., 1989). Previous theoretical studies (e.g., Hood & Priest, 1981; Kruskal et al., 1958; Shafranov, 1963) suggested that a MFR will be subject to kink instability once the total twist angle,  $\Phi$ , of its magnetic field lines exceeds a certain threshold, e.g.,  $2.5\pi$  radians for flux ropes in the solar atmosphere (Hood & Priest, 1981) with the confirmation by laboratory experiments (Myers et al., 2015). This threshold, however, is challenged by frequent observations of high-twist flux ropes not only in the solar atmosphere (e.g., Gary & Moore, 2004; Srivastava et al., 2010; Vršnak et al., 1991) but also in the heliosphere (e.g., Hu et al., 2015; Wang, Zhuang et al., 2016) and even in galaxies (e.g., Gómez et al., 2008; Marscher et al., 2008; Owen et al., 1989; Perley et al., 1984). The most recent statistical study of 115 interplanetary magnetic clouds near the Earth (Wang, Zhuang et al., 2016) showed that the total twist angle can be more than  $10\pi$  radians, much larger than the above theoretical thresholds, and its upper limit,  $\Phi_c$ , follows the relation given by Dungey and Loughhead (1954):

$$\Phi_c = 2 \frac{l}{R} \quad (1)$$

where  $l$  is the length of the MFR's axis and  $R$  is the radius of the MFR's cross section. Although a uniform-twist force-free flux rope model was used in Wang, Zhuang, et al.'s, (2016) study, the relation does suggest that a thinner and/or longer MFR can have higher-twisted magnetic field lines, or the inner core of a MFR can be more twisted, and does imply that a very long MFR, such as those in astrophysical jets, may be kink stable even though it is highly twisted.

However, in light of the magnetohydrodynamic theory, a linear force-free flux rope stays at a lower state of magnetic energy than a nonlinear force-free or nonforce-free flux rope with the same helicity. Thus, interplanetary magnetic clouds, which are considered to be the posteruption MFRs having relaxed for a sufficient period of time, were usually modeled as a linear force-free flux rope following Lundquist solution (Lepping et al., 2006; Lundquist, 1950), suggesting a minimum twist at the axis of the MFR and a maximum twist at the periphery. This is opposite to the implication from equation (1) that the inner core of a MFR can have a higher twist. This inconsistency raises the question of how the twist distributes in the cross section of a naturally hatched MFR, for example, those in CMEs, and is closely related to the long-standing debate whether or not a MFR forms prior to CME eruptions.

There are two competing scenarios about the onset of CMEs in terms of MFRs. One suggests that CMEs do not need a preexisting MFR, which can newly develop from sheared arcades through converging motion and magnetic reconnection during the course of the eruption (e.g., Antiochos et al., 1999; Karpen et al., 2012; Moore et al., 2001). The other believes that there must be a seed MFR, no matter how small it is, before the eruption (e.g., Kopp & Pneuman, 1976; Titov & Démoulin, 1999). The consensus is that the magnetic reconnection taking place beneath the erupting MFR will add a considerable amount of magnetic fluxes into the MFR by converting overlying field lines to the outer shell of the MFR (e.g., Qiu et al., 2007). If the seed MFR in the second scenario formed in a way similar to that in the first scenario through the magnetic reconnection of inner sheared arcades, the posteruption MFRs of the two scenarios might not be distinguishable (e.g., Aulanier et al., 2010). However, there are at least two other ways to generate a seed MFR in the solar atmosphere. One is the rotational/shearing motion of fluid elements on the photosphere, which are frozen into a bunch of closed magnetic field lines, and the other is the emergence of a MFR from the convection zone beneath the photosphere. Thus, the two scenarios may make the posteruption MFR quite different in terms of the distribution of twist. In the former case, the twist should increase from the axis to periphery of the MFR as illustrated by the cartoon in the paper by Moore et al. (2001). In the latter case, the twist might have a stage-like distribution in the cross section of the MFR, consisting of a core MFR and an outer shell with a different twist. Here another debate is whether the field lines added through reconnection are highly twisted (Aulanier et al., 2012; Longcope & Beveridge, 2007) or weakly twisted (van Ballegoijen & Martens, 1989).

In this paper, we present a rare event, in which an interplanetary magnetic cloud was sequentially observed by four spacecraft near the inner planets: Mercury, Venus, Earth, and Mars. By anatomizing the magnetic properties of the magnetic cloud at different heliocentric distance, we try to address the aforementioned debates, and refine the global picture of interplanetary magnetic clouds erupted from the Sun.

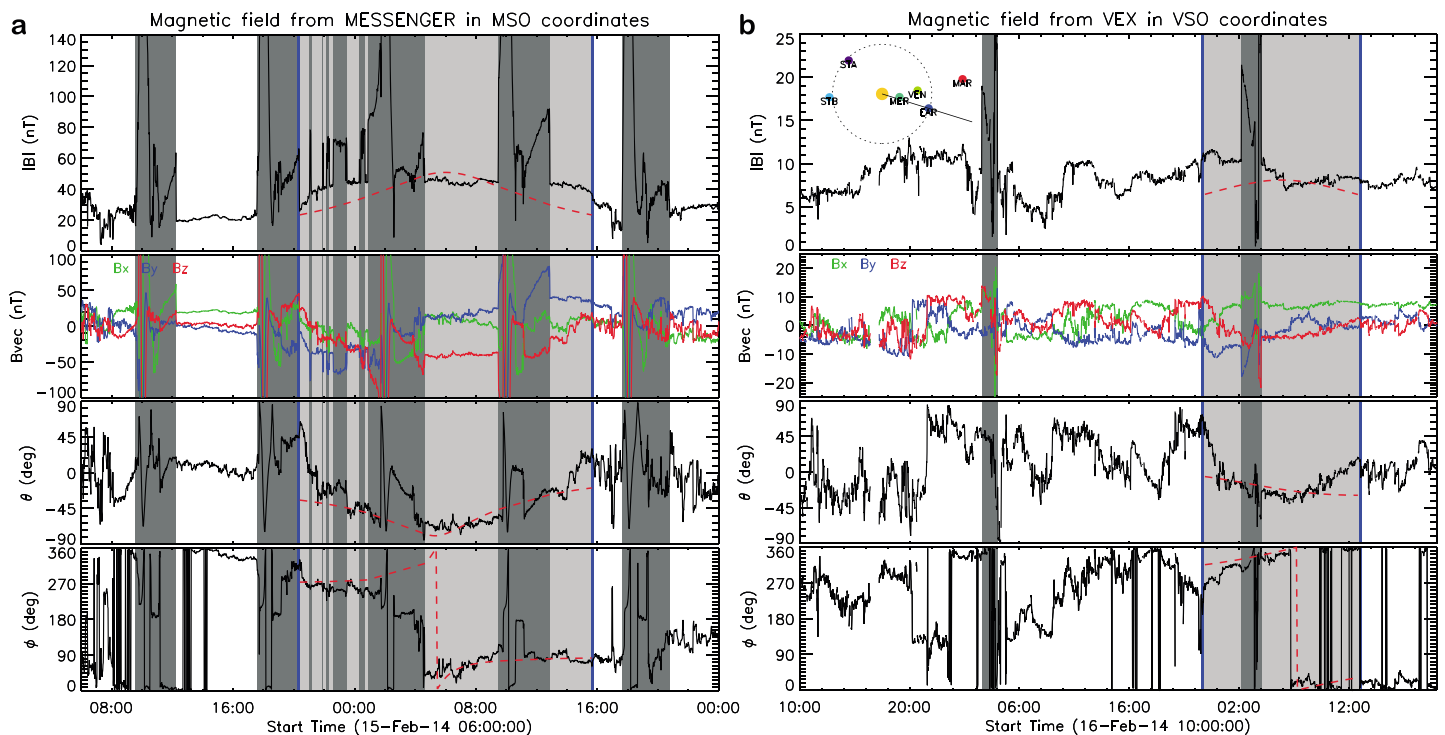


**Figure 1.** Magnetic fields measured by MErcury Surface, Space ENvironment, GEochemistry and Ranging (MESSENGER) (a) and VenUS EXpress (VEX) (b). In each panel, from the top to bottom, there are the total magnetic field strength,  $|B|$ , three components of  $\mathbf{B}$  in the planet-solar-orbital coordinate system, that is, Mercury solar orbital and Venus solar orbital coordinates for MESSENGER and VEX data, respectively, and the elevation,  $\theta$ , and azimuthal,  $\phi$ , angle of the  $\mathbf{B}$  vector. The dark-shadowed regions indicate the magnetosheath and magnetosphere behind the planetary bow shock. The magnetic cloud of interest is in the light-shadowed region bounded by two vertical blue lines. The red dashed lines are the fitting results by the velocity-modified uniform-twist force-free flux rope model (see section 3.1). The inset on the upper left corner of panel (b) shows the positions of the planets and spacecraft.

## 2. Overview of the Event

The cases of a magnetic cloud observed in situ by multiple spacecraft at different heliocentric distances were occasionally reported in the past 40 years (e.g., Burlaga et al., 1981; Du et al., 2007; Good et al., 2015; Leitner et al., 2007; Mulligan et al., 2001; Nakwacki et al., 2011; Nieves-Chinchilla et al., 2012; Winslow et al., 2016). The most famous one is the first identified magnetic cloud observed by Helios 1 and 2, IMP 8, and Voyager 1 and 2 in the inner and out heliosphere in January 1978 (Burlaga et al., 1981). However, that event is not suitable for our study, because the data are too poor. To our knowledge, there is a small number of well-observed events due to limited number of spacecraft in the heliosphere at same time, which were/are not necessarily well aligned along the radial direction.

### 2.1. The Magnetic Cloud at Mercury

The magnetic cloud in this study was first observed by the magnetometer on board the spacecraft MErcury Surface, Space ENvironment, GEochemistry and Ranging (MESSENGER, Anderson et al., 2007) orbiting around Mercury. Figure 1a shows the measurements of the magnetic field during 15–16 February 2014. Since Mercury owns a significant intrinsic magnetic field, it has a magnetosphere and a bow shock upstream (Slavin, 2004), and MESSENGER was immersed in pure solar wind for a limited time in its each  $\sim 8$  hr orbit. The regions within the magnetosheath and magnetosphere can be identified by the crossings of the bow shock, characterized by a sudden change in the magnetic field strength, as indicated by the dark-shadowed regions in the figure. The front boundaries of the dark-shadowed regions are the crossings close to the nose of the bow shock, and the rear boundaries locate at the flank. There are several spikes in the magnetic field strength during 15 February 20:00 UT to 16 01:00 UT, which were probably due to the swings of the bow shock disturbed by the passage of the magnetic cloud.

The magnetic cloud can be recognized between 15 February 20:20 UT and about 15:40 UT on the next day as indicated by the light-shadowed region bounded by two vertical blue lines in Figure 1a. Without those dark-shadowed regions, the signatures of a typical magnetic cloud are evident, including enhanced magnetic field strength (up to more than 45 nT compared with the field less than 25 nT before the cloud) and the large

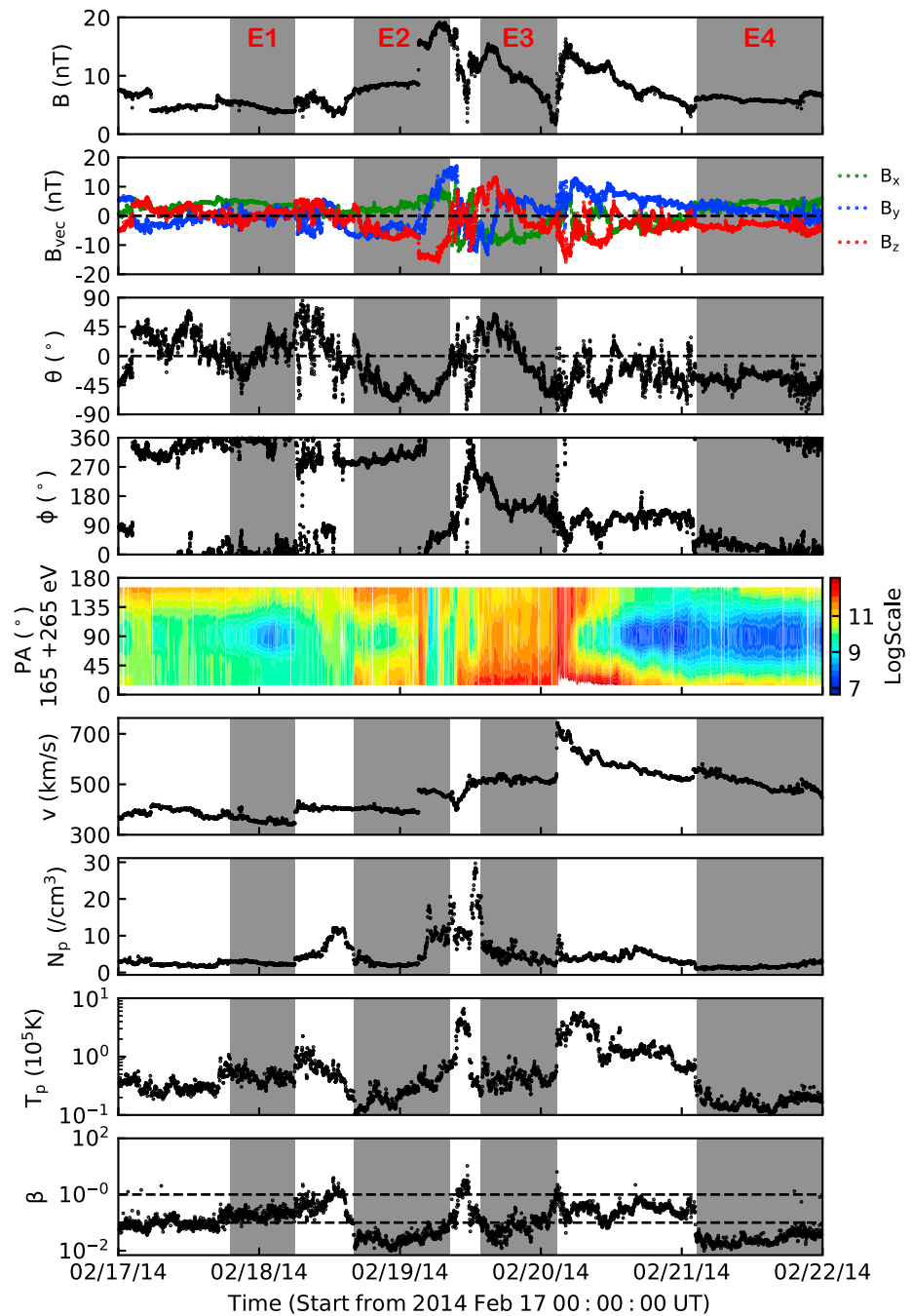


**Figure 2.** Observations of the magnetic cloud recorded by the Wind spacecraft at the Earth. From the top to bottom, it shows the total magnetic field strength,  $|B|$ , the three components of  $\mathbf{B}$  in geocentric solar equatorial coordinates, the elevation,  $\theta$ , and azimuthal,  $\phi$ , angle of the  $\mathbf{B}$  vector, the pitch angle distribution of suprathermal electrons, the bulk velocity,  $v$ , of the solar wind, and the number density,  $N_p$ , temperature,  $T_p$ , and plasma  $\beta$  of protons. The four shadow regions indicate four ejecta, labeled as E1 through E4.

and smooth rotation of the field vector. Unfortunately, there are only sporadic measurements of solar wind plasma, and therefore, we do not include them here. Despite some small data gaps due to the passages of Mercury's magnetosheath and magnetosphere, neither a strong driven shock which is typically accompanied by a narrow and highly fluctuated shock sheath, nor a wide shock sheath which usually follows a weak shock, could be found outside of either end of the cloud. Thus, the cloud should travel with a speed comparable to the ambient solar wind, consistent with the nearly symmetric profile of the magnetic field shown in the first panel of Figure 1a.



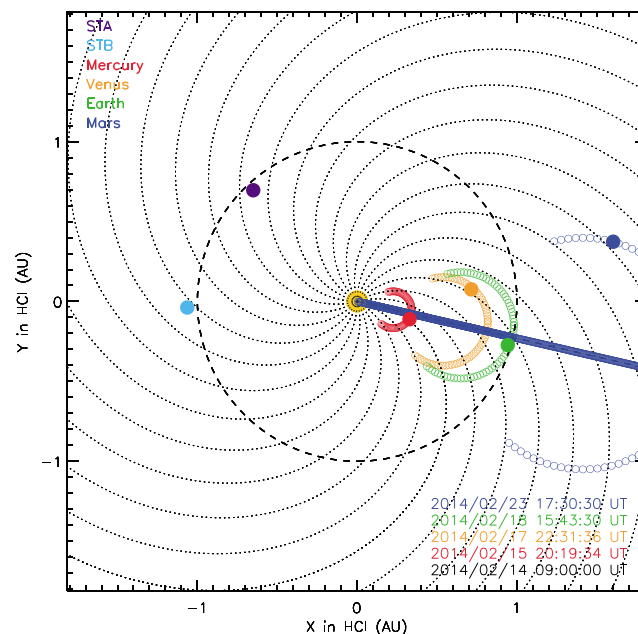


**Figure 3.** Trajectory of the magnetic cloud front on the ecliptic plane in the heliocentric inertial coordinates (HCI) estimated by the Deflection in InterPlanetary Space (DIPS) model (see section 2.3). The red, orange, green, and blue dots mark the positions of Mercury, Venus, Earth, and Mars, respectively, at the times of the magnetic cloud encountering them which have been given at the lower-right corner. The purple and azure dots indicate the positions of the Solar Terrestrial Relations Observatories (STEREO) A and B, respectively. The magnetic cloud front on the ecliptic plane is modeled by a circular arc with its two ends tangential to two radial directions between which the angle indicates the angular width of the magnetic cloud.

## 2.2. The Magnetic Cloud at Earth

Before identifying the counterpart of the magnetic cloud at Venus, we check its signature at the Earth, because Earth was well aligned with the Sun and Mercury (about  $2.6^\circ$  apart away from Mercury) at that time (see the inset at the upper left corner of Figure 1b or Figure 3) and the Wind spacecraft (Lepping et al., 1995; Ogilvie et al., 1995) near the Earth has complete sets of the interplanetary magnetic field and solar wind plasma data. Figure 2 shows the measurements in 5 days from 17 to 21 February. Combining the signatures of a CME ejecta, such as enhanced magnetic field strength, smooth rotation of field vector, low temperature, low proton  $\beta$ , and bidirectional suprathermal electron beams, etc., we may find four ejecta marked by “E1” through “E4” in the shadowed regions. Ejecta E1 arrived at the Earth at about 19:00 UT on 17 February. Considering that the distance between the Earth and Mercury is about 0.65 AU, we can estimate that the transit time of E1 is about 46.7 hr corresponding to a transit speed of about 580 km/s, which is much higher than its in situ speed of about 370 km/s. If E1 was the counterpart of the magnetic cloud observed by MESSENGER, it must have experienced a great deceleration, and can be estimated to have a speed about 800 km/s near Mercury. Such a fast ejecta should drive a strong shock as well as a shock sheath, which was not observed. Thus, E1 cannot be the counterpart of the magnetic cloud. The same analysis on ejecta E3 and E4 suggests that their expected transit speeds are 300 and 210 km/s, respectively, much lower than the in situ speeds, both faster than 500 km/s. Thus, the two ejecta are also not the counterpart of the magnetic cloud. As to ejecta E2 arriving at about 16:10 UT on 18 February, the expected transit speed is about 400 km/s, well consistent with the in situ speed measured by the Wind. Thus, it should be the same magnetic cloud observed at Mercury, unambiguously. The association can be further confirmed, as the counterparts of ejecta E1, E3, and E4 at Mercury as well as their corresponding CMEs can all be identified (we put the detailed identification process in Appendix A to make the main text fluent).

Ejecta E2 has clear signatures of a magnetic cloud. The rotation of the magnetic field was evident and smooth, the pitch angle of the suprathermal electrons concentrated around  $0^\circ$  and  $180^\circ$ , and the proton  $\beta$  was lower than 0.1. The rear part of the magnetic cloud was compressed by a strong forward shock, driven by ejecta E3, which destroyed the signature of the bidirectional electron beams.

**Table 1***Magnetic Properties of the Magnetic Cloud at Different Distances*

	$r$ (AU)	$(\theta, \phi)$ (deg)	$ d $ ( $R_{MC}$ )	$F_z$ ( $\times 10^{20}$ Mx)	$\tau$ (turns/AU)	$\tau_{AU}$ (turns/AU)	$h_{m,AU}$ ( $\times 10^{40}$ Mx <sup>2</sup> )	$D_{im}$ (%)
Mercury	0.35	(−65, 15)	$0.18^{+0.25}_{-0.10}$	$11.0^{+5.8}_{-5.3}$	$-3.8^{+1.9}_{-2.5}$	$-1.3^{+0.7}_{-0.9}$	$-160^{+79}_{-108}$	$15.2^{+5.8}_{-7.2}$
Venus	0.72(0.84)	(−52, 333)	$0.58^{+0.04}_{-0.08}$	$2.1^{+1.0}_{-0.9}$	$-6.9^{+3.5}_{-2.8}$	$-2.4^{+1.2}_{-1.0}$	$-10.6^{+6.1}_{-4.4}$	$76.8^{+8.2}_{-7.8}$
Earth	1.0	(−21, 356)	$0.54^{+0.10}_{-0.11}$	$1.0^{+0.6}_{-0.6}$	$-6.4^{+3.1}_{-5.4}$	$-6.4^{+3.1}_{-5.4}$	$-5.1^{+3.6}_{-3.0}$	$25.2^{+21.8}_{-17.2}$

*Note.* Column 2: The heliocentric distance of the planets during the period of interest. The value of 0.84 in the brackets is the position of the nose of the magnetic cloud when the cloud encountered Venus as shown in Figure 3. Column 3: The orientation, that is, the elevation and azimuthal angles, of the axis of the magnetic cloud in the planet-solar-orbital coordinate system, that is, Mercury solar orbital, Venus solar orbital, and geocentric solar equatorial coordinates for MESSENGER, VEX, and Wind, respectively. The uncertainty in the orientation is less than 10°. Column 4: The closest approach of the observational path to the axis of the cloud in units of the radius,  $R_{MC}$ , of the cloud. Column 5: The axial magnetic flux. Column 6: The number of turns per AU of the magnetic cloud field lines. Column 7: The corresponding  $\tau$  when the magnetic cloud arrives at 1 AU, which is given by  $\tau_{AU} = \frac{\tau}{r_{AU}}$  (see section 3.3). Column 8: The magnetic helicity per AU at the distance of 1 AU, given by  $h_{m,AU} = \tau_{AU} F_z^2$ . Column 9: The degree of the imbalance of the azimuthal flux. The values for Mercury and Venus are calculated from equation (8) and that for the Earth from equation (7).

### 2.3. The Magnetic Cloud at Venus

Venus locates between the Earth and Mercury at 0.72 AU. It was not well aligned with the two planets during the period of interest, but in a close angular position. The angular separation of Venus and Mercury was about 25° at the times when the magnetic cloud was passing through them. We may expect to observe the same magnetic cloud between 16 and 18 February. Similar to the situation at Mercury, there are only scattered measurements of pure solar wind plasma by Venus EXpress (VEX, Svedhem et al., 2007) and sometimes VEX located behind the bow shock and in the Venus-induced magnetosphere. The magnetic field data from the VEX magnetometer (Zhang et al., 2006) suggest that the interval between 17 February 22:40 UT and 18 February 13:00 UT is the only possible candidate, during which the long and smooth rotation of magnetic field vector is evident (see Figure 1b).

One may question that, if this structure is the same magnetic cloud, why did the magnetic cloud spend about 50 hr to travel from Mercury to Venus (a distance of ~0.37 AU) but less than only 18 hr from Venus to the Earth (a distance of ~0.28 AU). This is likely due to the curved front of the magnetic cloud (Möstl & Davies, 2013; Shen et al., 2014). By assuming a certain propagation speed of the magnetic cloud, we may model the arrival times of the magnetic cloud at different distances as shown in Figure 3. The model used in the study was developed for the CME Deflection in InterPlanetary Space (DIPS model; Wang et al., 2004; Wang, Zhang et al., 2016; Zhuang et al., 2017). The input parameters include the propagation speed, angular width and initial propagation direction of the CME, and the speed of background solar wind. In this study, we set the speeds of both the magnetic cloud and solar wind constant as 400 km/s because the transit speed of the magnetic cloud from Mercury to the Earth is 400 km/s, very close to the background solar wind speed measured by Wind, indicating little momentum exchange between the cloud and solar wind. The angular width and initial propagation direction are adjusted to obtain the best matched case, which is found to be about 60° and right facing to the Earth. The circular arcs in Figure 3 approximate the front of the magnetic cloud, of which the two ends are tangent to two 60° separated lines, respectively, starting from the Sun. Please note that the arcs just model the front of the cross section of the magnetic cloud cut by the ecliptic plane, but not the front of the global magnetic cloud structure, as implied by the modeled orientation of the cloud (see Table 1). It is revealed that the observed arrivals at Mercury, Venus, and the Earth can be well matched when the magnetic cloud propagated along the Sun-Mercury-Earth line and the angular width is about 60°.

### 2.4. Extrapolating the Trajectory of the Magnetic Cloud to Mars and Back to the Sun

Mars locates at about 1.65 AU around that time. By extrapolating the trajectory of the cloud to the orbit of Mars, we may predict that the arrival of the magnetic cloud at Mars was about 17:30 UT on 23 February, when it was only 7° apart away from Venus or 32° from Mercury by comparing their positions at the times when the cloud is crossing them. Unfortunately, there was no appropriate instrument measuring the interplanetary magnetic field or the solar wind plasma near Mars. The only useful data are from the Radiation Assessment Detector (RAD, Hassler et al., 2012) on board Mars Science Laboratory (MSL, Grotzinger et al., 2012), providing the information of Forbush decreases, which are believed to be caused by the passage of CMEs (Cane, 2000). Figure 4 shows the dose rate of cosmic rays recorded by the RAD from 15 February to 5 March, during which

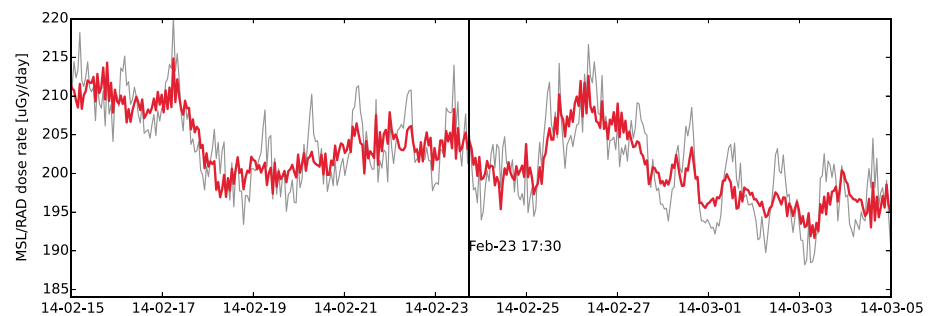


**Figure 4.** The dose rate of the cosmic rays observed by Radiation Assessment Detector on board the Mars Science Laboratory at Mars. The gray line marks the original data which shows a daily periodic variation caused by the diurnal Martian atmospheric thermal tide (Guo et al., 2017). The red line represents the data when applied a frequency filter to remove the diurnal variations therein (Guo et al., 2018). The vertical line marks the predicted arrival of the magnetic cloud at Mars.

several Forbush decreases are evident. The predicted arrival of the magnetic cloud perfectly corresponds to the beginning of a decrease as marked by the vertical line. According to the Wind observations, there were several faster ejecta catching up with the magnetic cloud of interest. Thus, it is very possible that these ejecta interacted with each other and formed a complex structure before arriving at Mars to make such a significant Forbush decrease.

Similarly, we may extrapolate the trajectory of the magnetic cloud back to the Sun. The predicted onset time of the corresponding CME is 09:00 UT on 14 February. However, the magnetic cloud was a slow and therefore weak one, whereas the Sun was quite active around that period from 13 to 15 February, during which many larger and stronger CMEs were launched. Thus, the identification of the CME corresponding to the magnetic cloud in coronagraphs is more or less ambiguous, and no definite eruptive signature on the solar surface can be found around the expected time, suggesting the possibility of a stealth CME. The detailed process of our identification is given in Appendix B.

### 3. Magnetic Evolution of the Magnetic Cloud From Mercury to Earth

#### 3.1. Reconstruct the Magnetic Cloud With the Uniform-Twist Force-Free Flux Rope Model

The observations of the same magnetic cloud at different heliocentric distance provide us a unique opportunity to study the magnetic properties of the cloud and their changes with the distance. There are various techniques to reconstruct a magnetic cloud from one-dimensional measurements along the observational path (e.g., Burlaga et al., 1981; Cid et al., 2002; Dasso et al., 2006; Goldstein, 1983; Hidalgo et al., 2002; Hu & Sonnerup, 2002; Lepping et al., 1990; Marubashi, 1986; Mulligan & Russell, 2001; Vandas & Romashets, 2003; Wang et al., 2015; Wang, Zhuang et al., 2016). Cylindrical force-free flux rope models are frequently used and tested to be reliable (Riley et al., 2004). Here we choose the velocity-modified uniform-twist force-free flux rope model (Wang, Zhuang et al., 2016) to fit the observed data, which treat the magnetic twist as a free parameter in the fitting procedure. The Grad-Shafranov (GS) reconstruction technique (Hu & Sonnerup, 2002) can also obtain the twist of a magnetic cloud, but it needs more solar wind plasma parameters, including the total gas pressure and therefore cannot be applied to the MESSENGER and VEX data.

The fitting model we used has 10 free parameters: the magnetic field strength at the flux rope's axis ( $B_0$ ), the orientation of the axis (the elevation and azimuthal angles,  $\theta$  and  $\phi$ , in geocentric solar equatorial coordinates), the closest approach of the observational path to the axis ( $d$ ), three components of the propagation velocity ( $v_x$ ,  $v_y$ ,  $v_z$ ), the expansion speed ( $v_{\text{exp}}$ ) and poloidal speed ( $v_{\text{pol}}$ ) at the boundary of the flux rope, and importantly, the twist. These free parameters are coupled, and we constrain them with both the measurements of magnetic field and solar wind velocity. Although there is no data of solar wind velocity from the MESSENGER and VEX, we may assume that the magnetic cloud propagated at a constant speed of 400 km/s without expansion, which is reasonable based on the above DIPS model result and the flattened profile of the radial velocity recorded by Wind at 1 AU. The influence of the nonexpansion assumption on the fitting results is tested for the magnetic cloud at Mercury by setting an expansion speed of about 20 km/s, which is small (see Appendix C). The time resolution of the data input to our model is set to 5 min. The detailed description of the fitting technique of this model can be found in our recent paper (Wang, Zhuang et al., 2016).

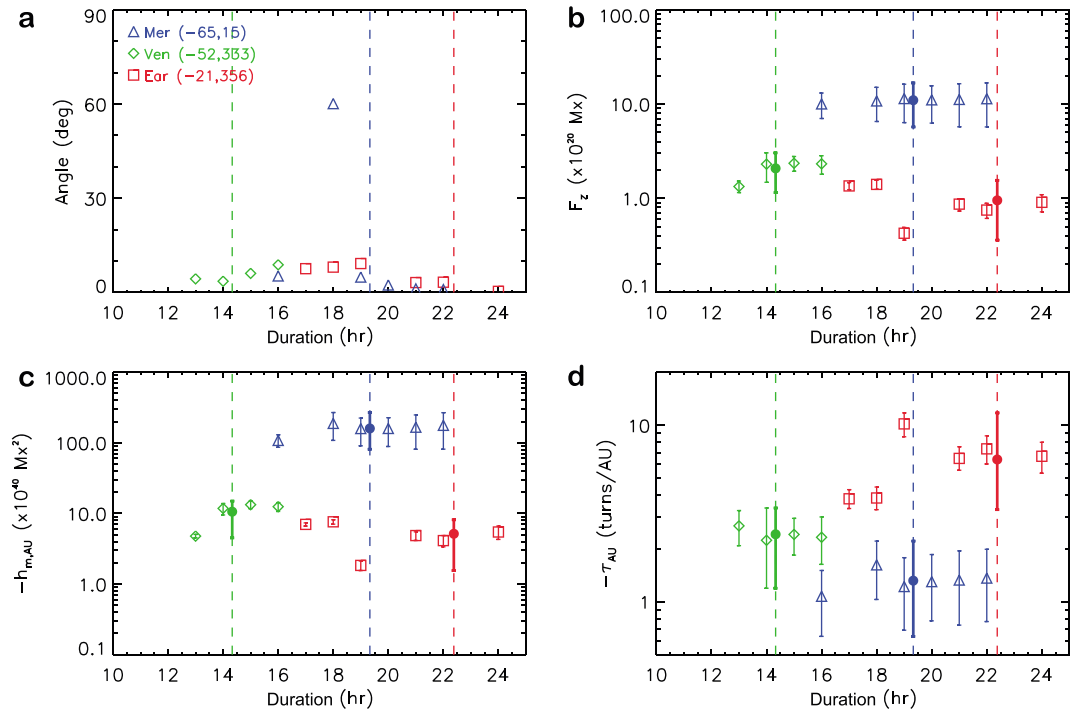


**Figure 5.** Fitting parameters of the magnetic cloud as a function of the boundary (see section 3.1). The horizontal axis indicates the duration from the front boundary to the rear boundary of the magnetic cloud, and the vertical dashed lines denote the duration based on the identified boundaries of the cloud based on the observations with the blue, green, and red colors (or triangle, diamond, and square symbols) for the cloud at Mercury, Venus, and the Earth, respectively. Each symbol stands for a test fitting with a pair of different front and rear boundaries. (a) The angle between the orientation (defined by  $\theta$  and  $\phi$  in the planet-solar-orbital coordinates) of the axis of the magnetic cloud from each test fitting and the overall averaged orientation of the axis, which is listed in the upper left corner. (b–d) The values of the axial magnetic flux,  $F_z$ , the magnetic helicity per unit length,  $h_{m,AU}$ , and the number of twist per unit length,  $\tau_{AU}$ . The subscript “AU” means that the parameters are rescaled to the values at the distance of 1 AU (see section 3.3 for more details). The solid dots mark the average of the symbols with the same color, and the error bars of the dots cover the uncertainties of the symbols.

As indicated by the name of the model, the twist is assumed to be uniform in the cross section of a flux rope. This is a good approximation to most magnetic clouds. In Hu et al. (2015), it was shown that the twist is probably high near the axis of a MFR and then quickly drops to a lower value when moving away from the axis, which suggested that the twist is almost uniform in most part of a MFR except that the place is very close to its axis. The observational work about a solar eruption by Wang et al. (2017) reached a similar conclusion. Even if a magnetic cloud carries an irregular twist profile, our model will give a kind of averaged twist over the shell of the cloud crossed by the spacecraft, which could be treated as a first-order approximation. If the spacecraft at the different planets crossed the cloud with different impact distances to its axis, we may anatomize how the twist distributes in the cloud.

The most important free parameter in the fitting is the orientation of the magnetic cloud’s axis, which can affect the reliability of other fitting parameters. One major factor influencing the orientation is the location of the boundary of the cloud, which is difficult to be precisely determined. Thus, to test the reliability of the fitting, we run test fittings by moving the front and rear boundaries simultaneously inward or outward with the same interval, and get a set of test fitting results. Not all of the fittings are successful. The quality of a fitting result can be assessed by the combination of the normalized root-mean-square ( $\chi_n$ ) of the difference between the modeled and observed data and a set of three quantities related to the twist: the percentage (per) of the data points falling in the uncertainty range of the modeled twist, the correlation coefficient (cc) of the modeled and measured twists, and the confidence level (cl) of the correlation (see section 2.2 on p. 9324 of Wang, Zhuang et al., 2016 for more details). In this study, we set a criterion of  $\chi_n \leq 0.6$ , per  $\geq 0.4$ , cc  $\geq 0.4$ , and cl  $\geq 0.9$  for an acceptable fitting. Figure 5 shows the test fitting results, in which only the fittings satisfying the criterion are displayed. According to these successful fittings, the orientations of the magnetic cloud axis

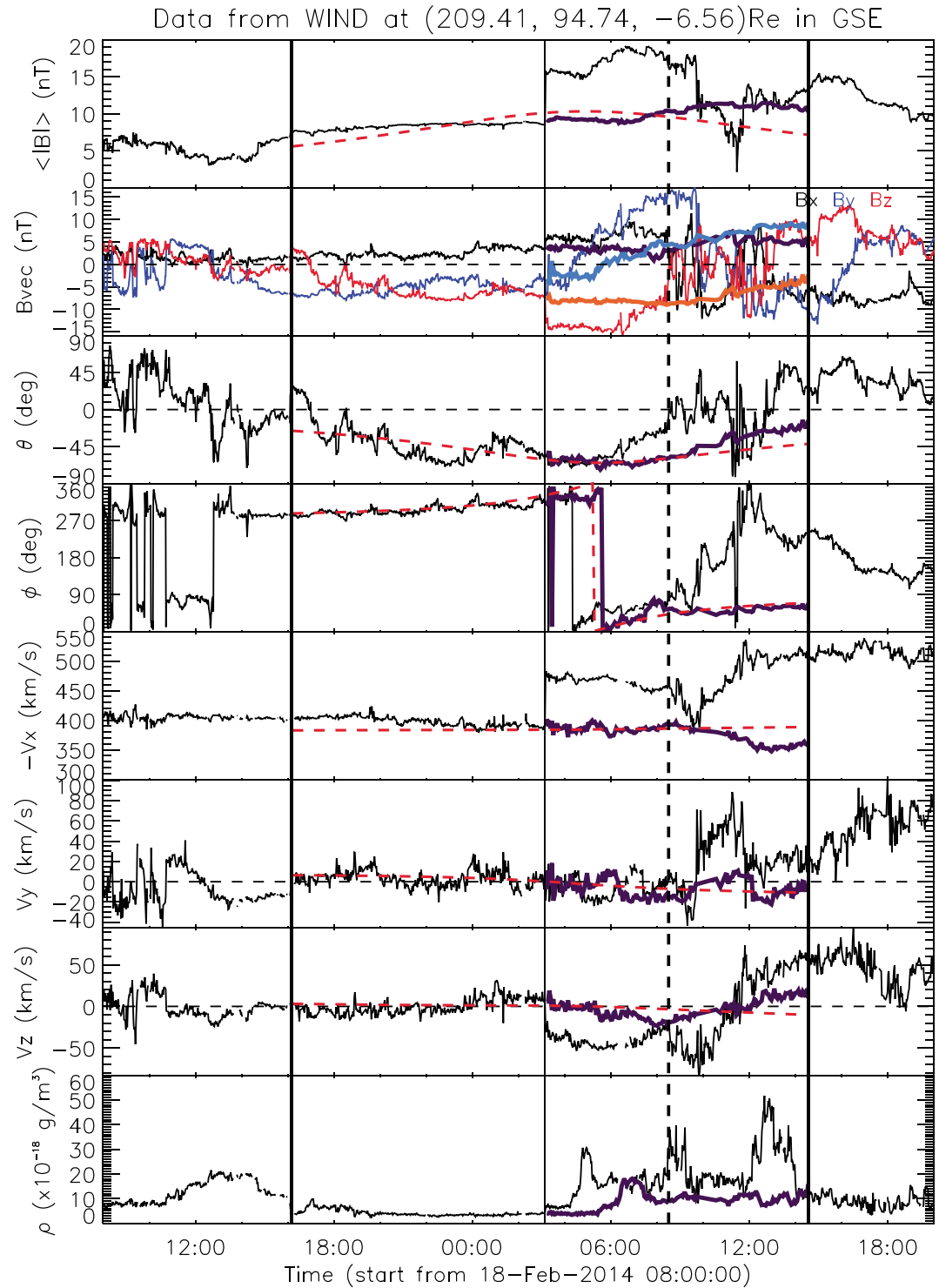


**Figure 6.** Zoom-in plot for ejecta "E2" observed at Earth. The first and last vertical lines mark the front and rear boundaries of the recovered magnetic cloud, and the vertical dashed line indicates the original rear boundary of the cloud. The second vertical line marks the shock surface. The thick curves between the second and last vertical lines represent the recovered structure, which originally locates between the second and third vertical lines (see section 3.2). The duration of the recovered structure is determined by equation (3). The red dashed curves are the fitting results.



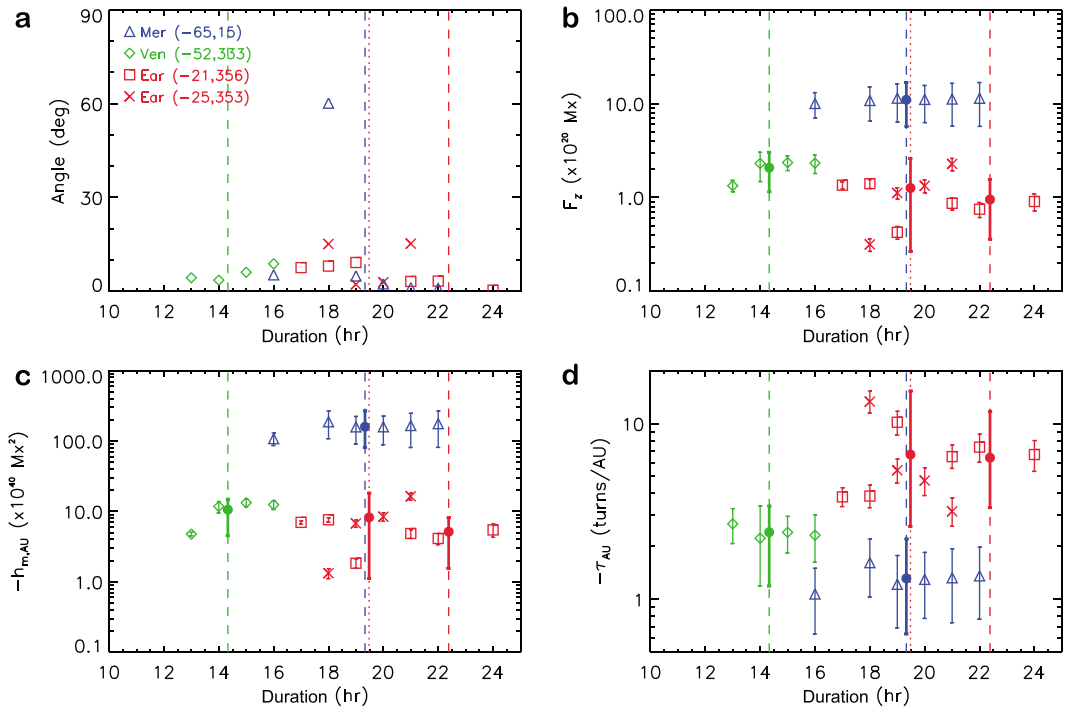


**Figure 7.** Same as Figure 5 except that the fitting results of the magnetic cloud at the Earth by changing the uniform compression ratio to the linearly decreasing compression ratio are added as cross symbols for comparison. The red dotted vertical line indicates the duration of the magnetic cloud by using the new compression ratio.

derived based on different boundaries (see Figure 5a) concentrate to a certain value with differences less than about  $10^\circ$  (with only one exception for the fitting to the MESSENGER data, which is omitted in determining the final orientation below), suggesting a high reliability of the fitting result. The final orientation of the magnetic cloud axis at each distance is the average of the orientations of the successful test fittings (as listed in Table 1). The red dashed lines in Figures 1 and 6 are the fitting curves obtained based on the final orientations.

It should be noted that the magnetic cloud observed at the Earth, which was partially compressed by an overtaking shock, cannot be fitted directly. We recover the shocked structure before applying the fitting technique by assuming that the parameters in the shock sheath still follow the shock relation. Though it is a very ideal approximation, the fitting results seem to be reliable. The next subsection gives the details.

### 3.2. Recover the Shocked Structure

The shock arrived at Wind at 03:10 UT on 19 February, and the shock sheath spanned over about 6.5 hr, of which the first 5.3-hr interval located inside the magnetic cloud. To apply a fitting technique to the magnetic cloud, the shocked part of the magnetic cloud has to be recovered back to the uncompressed state. To accomplish this purpose, we assume that (1) the magnetic field, plasma velocity, and density in the sheath region can be related to the uncompressed state by the shock relation, that is, Rankine-Hugoniot jump conditions, and (2) the shock normal,  $\hat{n}$ , shock speed,  $v_s$ , and the compression ratio,  $r_c$ , are the same as those at the observed shock surface. Treating the sheath region as the downstream (using subscript “2”) of the shock, the uncompressed state, that is, the parameters of the upstream (using subscript “1”) of the shock, can be given by

$$\begin{cases} \rho_1 = \frac{1}{r_c} \rho_2 \\ \mathbf{B}_{1n} = \mathbf{B}_{2n} \\ \mathbf{B}_{1\perp} = \frac{v_{A2}^2 - u_2^2}{v_{A2}^2 - r_c u_2^2} \mathbf{B}_{2\perp} \\ \mathbf{u}_{1n} = r_c \mathbf{u}_{2n} \\ \mathbf{u}_{1\perp} = \frac{v_{A2}^2 - u_2^2}{v_{A2}^2 - r_c u_2^2} r_c \mathbf{u}_{2\perp} \end{cases} \quad (2)$$

in which  $\rho$  is the density including the protons and electrons,  $\mathbf{B}$  is the magnetic field with the subscript “ $n$ ” (“ $\perp$ ”) parallel (perpendicular) to the shock normal,  $\mathbf{u}$  is the solar wind speed in the DeHoffman-Teller (HT) frame, and  $v_A = \sqrt{\frac{B^2}{\mu\rho}}$  is the Alfvén speed. The recovered interval is longer than the shocked interval, and its duration is calculated by using the formula

$$dt_1 = \frac{u_{2n} + v_s}{u_{1n} + v_s} r_c dt_2 \quad (3)$$

based on the mass conservation. The recovered parameters are plotted in Figure 6.

The shock parameters,  $\hat{\mathbf{n}}$ ,  $v_s$ , and  $r_c$ , are obtained by using a nonlinear least squares fitting technique (Szabo, 1994; Viñas & Scudder, 1984) based on the incomplete Rankine-Hugoniot conditions. A total of 10 data points with time resolution of 92 s between 03:00:18 UT and 03:18:11 UT on 29 February are used in the fitting. The calculated shock normal is  $(-0.93, -0.01, -0.37)$  in geocentric solar equatorial coordinates, the shock speed is  $v_s = 585$  km/s in the spacecraft frame, and the compression ratio is 1.69.

The assumptions in recovering the shocked structure are highly ideal. Particularly, the compression ratio in the sheath region cannot be the same. To check the influence of the compression ratio on the fitting result of the magnetic cloud at the Earth, we replace the uniform  $r_c$  in the sheath region with a varying  $r_c$  linearly decreasing from 1.69 at the shock surface to 1.0 in the following 6.5-hr duration. Using the same technique described above, we fit the recovered magnetic cloud. The results, indicated as cross symbols in Figure 7, are consistent with those (the square symbols) by using the uniform  $r_c$ , and do not change the conclusion we will reach below. This suggests that the ideal assumptions are acceptable for this study.

### 3.3. Results

Three fitting parameters are investigated to study the changes of the magnetic properties of the magnetic cloud, which are the axial magnetic flux,  $F_z$ , the number of turns per AU,  $\tau$ , and the magnetic helicity per AU,  $h_m$ . The axial magnetic flux and total magnetic helicity are two invariant parameters for magnetic clouds if no reconnection is involved with the surrounding magnetic field. This implies that  $\tau$  and  $h_m$  both depend on the length of the axis of the magnetic cloud. Thus, to make their values obtained at different distances comparable, we normalize them to the values when the magnetic cloud arrives at the distance of 1 AU. This normalization can be easily done under the reasonable assumption that the length of the axis of the magnetic cloud is proportional to the heliocentric distance,  $r$ . In other words, we can get the normalized values of  $\tau$  and  $h_m$  by using  $\tau_{AU} = \frac{r}{r_{AU}} \tau$ ,  $h_{m,AU} = \frac{r}{r_{AU}} h_m = \tau_{AU} F_z^2$ , respectively. For the magnetic cloud at Mercury, Venus, and the Earth, the value of  $r$  is 0.35, 0.84, and 1.0 AU, respectively. Note that the nose of the magnetic cloud was at 0.84 AU when the cloud arrived at Venus based on the DIPS model though Venus located at 0.72 AU (see Figure 3).

Figures 5b and 5c show the results of  $F_z$  and  $-h_{m,AU}$ , which fall in the typical range estimated in previous statistical studies (Wang et al., 2015). The averaged values and uncertainties of these parameters, which are calculated based on all the successful test fittings, are marked by the dots with error bars (and also listed in Table 1). It is found that  $F_z$  and  $-h_{m,AU}$  generally decrease from Mercury to the Earth. The averaged value of  $F_z$  at the Earth and Venus is about only 9% and 19% of that at Mercury, respectively. Similarly, the averaged value of  $-h_{m,AU}$  at the Earth and Venus is about only 3% and 7% of that at Mercury. If the uncertainty in the fitting parameters are considered, the decreases are still notable, which are at least 28% and 54%, respectively, in  $F_z$  and 10% and 19%, respectively, in  $-h_{m,AU}$ . In contrast, the derived twists at Mercury are obviously weaker than (or about 0.2 times of) those at the Earth as shown in Figure 5d, and the twists at Venus locate between.

## 4. Possible Interpretations for the Model Results

### 4.1. “Pancaking” Effect

There are several possible interpretations for the decreases of the axial magnetic flux and helicity and the increase of the twist as illustrated in Figure 8. First one is due to the “pancaking” effect (or called stretching effect, e.g., Crooker & Intriligator, 1996; Manchester et al., 2004; Riley & Crooker, 2004; Riley et al., 2003; Russell & Mulligan, 2002), which makes the cross section of a MFR deviated away from a circular shape (Figure 8a). Based on the theoretical analysis on the linear force-free field by Démoulin and Dasso (2009), it is suggested that the axial flux might be underestimated, say by a factor of  $a$ , if using a cylindrical model to fit a stretched cloud, but it will have little effect on the azimuthal flux. As a consequence, the ratio of the azimuthal flux

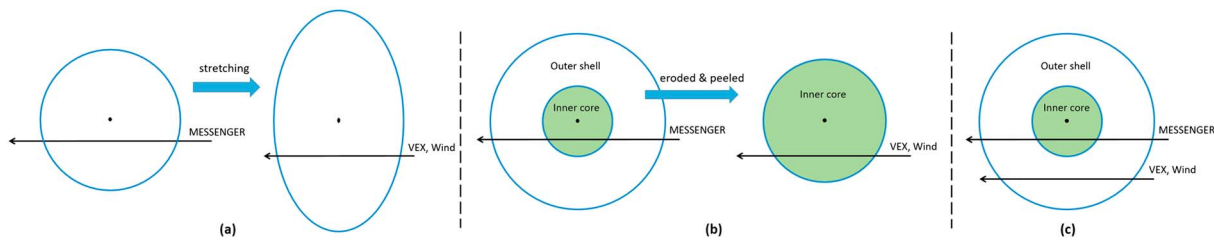


**Figure 8.** Schematic diagram showing three possible scenarios explaining the variations of the magnetic properties from Mercury to the Earth. In Scenario 1, the magnetic cloud was stretched, which may cause the axial flux underestimated and twist overestimated. In Scenarios 2 and 3, the magnetic cloud is roughly divided into two parts: an inner core and an outer shell. Scenario 2 suggests that there was a great erosion during the cloud propagated toward the Earth, and all the spacecraft passed through the inner core. Scenario 3 does not include a significant erosion, and only MESSENGER cut through the inner core according to the closest approaches of the observational path to the cloud's axis derived by the fitting method. The analysis suggests that Scenarios 1 and 2 could explain the observations (see sections 3.3 and 4.4 for more details).

per unit length to the axial flux, that is, a kind of averaged twist, will be overestimated by a similar factor. Thus, the decrease/increase of the axial flux/twist due to the pancaking effect is not real but from the model bias.

It should be noted that the twist in our model is not estimated based on the ratio of the azimuthal flux to the axial flux, but independently obtained by fitting to the measurements of  $\frac{B_\phi}{xB_z}$ , in which  $B_\phi$  and  $B_z$  are two components of the magnetic field in the magnetic cloud frame ( $r, \phi, z$ ) with  $z$  along the axis of the magnetic cloud and  $x$  is the distance from the cloud axis normalized by its radius  $R_{MC}$  (see the description in section 2.2 of Wang, Zhuang, et al., 2016). We can imagine that the pancaking effect can make  $R_{MC}$  underestimated by a factor of the order of  $\sqrt{a}$  but have little to do with  $\frac{B_\phi}{B_z}$ . Thus, the overestimation factor of the twist value by this method should be smaller than that by using the ratio of the two fluxes.

If the underestimation factor,  $a$ , in the axial flux was 11 at the Earth, this effect could well explain the decrease of the axial flux that is about 91% from Mercury to the Earth. However, when reaching the underestimation factor of 11, the magnetic cloud should have been highly stretched with the aspect ratio of its cross section of more than 10 according to Figure 9 in the paper by Démoulin and Dasso (2009). Some MHD numerical simulations showed that the aspect ratio is about 3 or less near 1 AU (see, e.g., Figure 3 in Riley et al., 2003 and Figure 5 in Manchester et al., 2004). Other simulations suggested that the pancaking effect is not so significant even if a magnetic cloud is compressed by a following fast shock and/or ejecta (see Figure 3 in Xiong et al., 2006 and Figure 1 in Xiong et al., 2007). Assuming that the aspect ratio of the stretched cross section of the cloud is 3, which is large enough according to those simulations, we may read from Figure 8 of Démoulin and Dasso (2009) that the underestimation factor of the axial flux is about 3.2, leading to its apparent decrease by about 69% from Mercury to the Earth, marginally explaining the derived decrease of the axial flux if the uncertainties in the derived fluxes are considered. Similarly, the increase of the twist from Mercury to the Earth may also be marginally explained by the pancaking effect with the uncertainties considered.

#### 4.2. "Erosion" Effect

It was suggested that magnetic clouds may experience erosion process (e.g., Dasso et al., 2006; Manchester et al., 2014; Ruffenach et al., 2012, 2015) through the magnetic reconnection with ambient solar wind (Gosling, 2012) when they propagate away from the Sun. A previous statistical study of 50 magnetic clouds (Ruffenach et al., 2015) showed that up to 90% of magnetic flux, with an average of 40%, can be eroded based on the imbalance of azimuthal magnetic flux in these clouds. A complete erosion process roughly consists of four phases as illustrated in Figure 9: a preerosion phase, during which the magnetic field lines of a magnetic cloud are not reconnected with the magnetic field lines in the ambient solar wind yet; an ongoing erosion phase, when the reconnection is taking place; a peeling-off phase, when the reconnected field lines are being peeled-off from the magnetic cloud; a posterosion phase, the eroded magnetic field flux has been completely peeled-off from the magnetic cloud. The second and third phases may happen simultaneously. Figure 8b shows an example of erosion by dividing the magnetic cloud into two parts: an inner core and an outer shell. The outer shell is gradually eroded during the propagation. The observational signature of the erosion of this event will be given later in section 4.4. Here we will see if this scenario can explain the decrease of the axial flux and the increase of the twist and if it is consistent with the observed profile of magnetic field from the spacecraft.

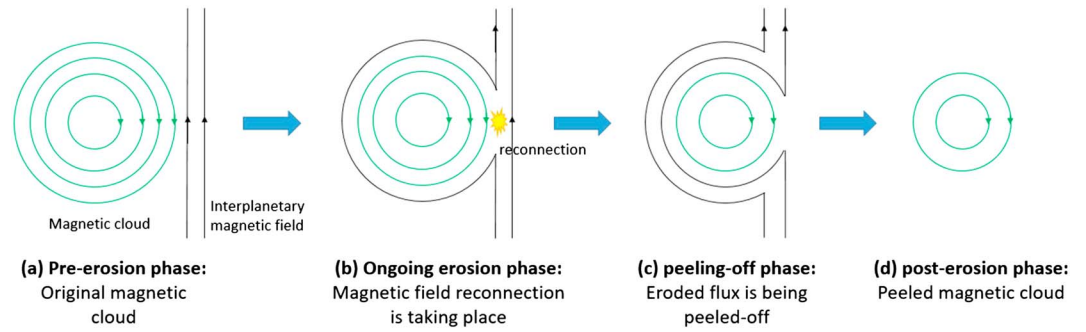


**Figure 9.** Schematic diagram showing four phases of a complete erosion process of a magnetic cloud: (a) preerosion phase, (b) ongoing erosion phase, (c) peeling-off phase, and (d) posterosion phase.

To better understand this scenario, the closest approach,  $d$ , of the observational path to the axis of the magnetic cloud derived from the fitting method is listed in Table 1 for reference. It is suggested that the MESSENGER spacecraft at Mercury was relatively much closer to the axis of the cloud than VEX at Venus and Wind at the Earth. Thus, all the spacecraft passed through the inner core of the magnetic cloud. Based on Figure 8b, we may assume that the boundary of the inner core initially locates between  $0.2R_{MC}$  and  $0.5R_{MC}$ , say at about  $0.4R_{MC}$ . Moreover, we assume that the magnetic fields in the inner core and the outer shell are roughly constant, setting to be  $B_{core}$  and  $B_{shell}$ , respectively. Then, the axial and poloidal magnetic fluxes and the twist derived from our uniform-twist flux rope model can be approximated as

$$\begin{cases} F_{z,M} = 2\pi [B_{core,z}R_{core}^2 + B_{shell,z}(R_{MC}^2 - R_{core}^2)] \\ F_{\varphi,M} = [B_{core,\varphi}R_{core} + B_{shell,\varphi}(R_{MC} - R_{core})]L \\ \tau_M = \frac{F_{\varphi,M}}{F_{z,M}L} = \frac{B_{core,\varphi}R_{core} + B_{shell,\varphi}(R_{MC} - R_{core})}{F_{z,M}} \end{cases} \quad (4)$$

if the spacecraft crossed the cloud with the closest approach like MESSENGER, and approximated as

$$\begin{cases} F_{z,E} = 2\pi (B_{core,z}R_{core}^2) \\ F_{\varphi,E} = B_{core,\varphi}R_{core}L \\ \tau_E = \frac{F_{\varphi,E}}{F_{z,E}L} = \frac{B_{core,\varphi}R_{core}}{F_{z,E}} \end{cases} \quad (5)$$

if the spacecraft crossed the cloud like Wind. Here  $L$  is the length of the axis of the cloud. Based on our model results (see Table 1), we roughly have  $\frac{F_{z,M}}{F_{z,E}} \approx 10$  and  $\frac{\tau_M}{\tau_E} \approx 0.2$ . From equations (4) and (5), we can deduce that  $B_{core} \approx \sqrt{(1.5B_{shell,\varphi})^2 + (0.58B_{shell,z})^2}$ , or  $0.58B_{shell} < B_{core} < 1.5B_{shell}$ . It suggests that the magnetic field is flattened from the inner core to outer shell, consistent with the magnetic field profile measured by MESSENGER as shown in the first panel of Figure 1a. Thus, this scenario can also explain the derived variations in the axial flux, helicity and twist, and differently from the pancaking effect, these variations are real.

### 4.3. Double-Layer Structure Without Erosion

Another possible scenario is as shown in Figure 8c, in which the magnetic cloud is also considered as a combination of an inner core and an outer shell as the previous scenario. But in this case, there was no significant erosion happening to the cloud, and VEX and Wind only cut through the outer shell of the magnetic cloud in contrast to MESSENGER which crossed through its inner core. This scenario might also explain the decrease of the axial flux and increase of the twist if the inner core carries a stronger magnetic field and a weaker twist than the outer shell. However, the similar analysis of the values of  $B_{core}$  and  $B_{shell}$  presented below disapproves the possibility.

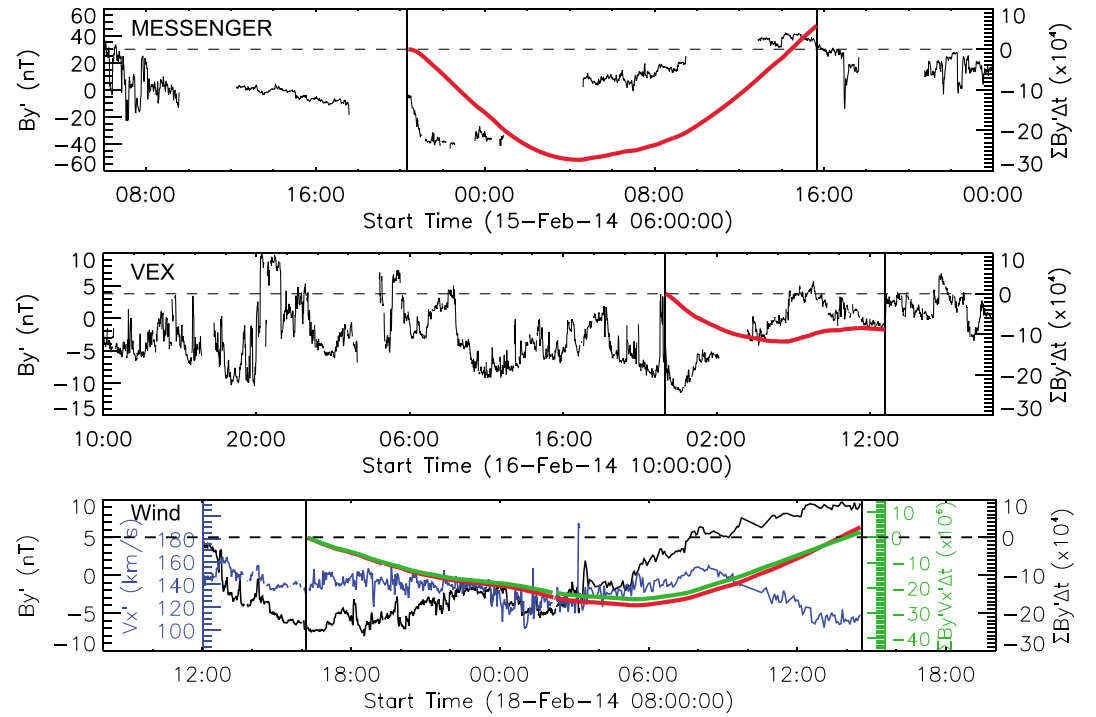


**Figure 10.** Imbalance of the azimuthal magnetic flux. The black curves in all the panels show the profiles of the  $y'$  component of the magnetic field in the magnetic cloud frame ( $x', y', z'$ ) with  $z'$  along the axis of the magnetic cloud and  $y'$  perpendicular to the plane defined by  $z'$  and the observational path of the spacecraft. The blue curve in the last panel shows the profile of the  $x'$  component of the solar wind velocity, and is scaled by the second vertical axis on the left. The vertical lines mark the boundary of the magnetic cloud. The thick red lines give the profile of the cumulative value of  $B_{y'} v$  with the time by using equation (8), and the thick green line the profile of the cumulative value of  $B_{y'} v_{x'}$  by using equation (7). All these thick lines have been corrected to the values when the cloud arrives at 1 AU by multiplying the distance ratio  $\frac{r}{r_{AU}}$  as what we did to  $h_m$  and  $\tau$ , and the scales are given by the vertical axes on the right in the units of (nT s) for the red lines or (nT km) for the green line. The deviation of the right ends of these thick lines away from zero indicates a possible imbalance.

In this scenario, equation (5) should be revised as

$$\begin{cases} F_{z,E} = 2\pi (B_{shell,z} R_{MC}^2) \\ F_{\varphi,E} = B_{shell,\varphi} R_{MC} L \\ \tau_E = \frac{F_{\varphi,E}}{F_{z,E} L} = \frac{B_{shell,\varphi} R_{MC}}{F_{z,E}} \end{cases} \quad (6)$$

and the relation between  $B_{core}$  and  $B_{shell}$  becomes  $B_{core} \approx \sqrt{(3.5B_{shell,\varphi})^2 + (57B_{shell,z})^2}$ , or  $3.5B_{shell} < B_{core} < 57B_{shell}$ , suggesting a much stronger magnetic field in the inner core than in the outer shell. It does not match the magnetic field profile measured by MESSENGER or Wind.

#### 4.4. Signatures of the Erosion Process Possibly Experienced by the Magnetic Cloud

Both the pancaking and erosion effects may explain the variations of the derived magnetic properties. However, it is difficult to assess how significant the pancaking effect was based on the one-dimensional data. Here we focus on the erosion effect to look for observational signatures. A frequently used signature is the imbalance of azimuthal magnetic flux of magnetic clouds. The azimuthal magnetic flux is calculated in the magnetic cloud frame ( $x', y', z'$ ) with  $z'$  axis along the orientation of the axis of the cloud and  $y'$  axis perpendicular to both  $z'$  axis and the observational path of the spacecraft. The measured magnetic field and solar wind velocity are then projected onto the ( $x', y'$ ) plane. For a complete MFR, the azimuthal magnetic flux cumulated from one boundary of the MFR to the other along the observational path should be zero. A deviation from zero is the imbalanced flux,  $F_{im}$ , estimated as

$$\frac{F_{im}}{L} = \int_{in}^{out} B_{y'} v_{x'} dt \quad (7)$$



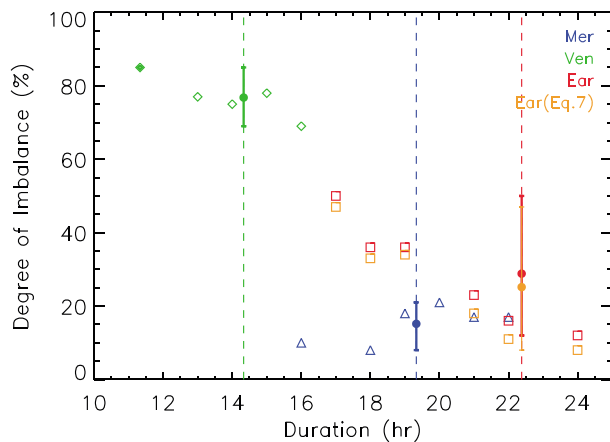


**Figure 11.** Degree of the imbalance of the azimuthal flux for the cloud with different boundaries. The symbols follow the same meaning as those in Figure 5. For the cloud at Venus, we add an additional test case by moving front boundary of the cloud inward by 3 h as shown by the filled green diamond. The imbalances at Earth calculated based on equations (8) and (7) are displayed by the symbols in red and orange, respectively.

in which  $L$  is the length of the MFR,  $B_y$ , and  $v_{x'}$  are the measured magnetic field and solar wind speed along the  $y'$  and  $x'$  directions, respectively, in the magnetic cloud frame, and *in* and *out* indicate the integral through the front boundary of the cloud to the rear boundary. The imbalance of azimuthal flux provides evidence of eroded but not yet peeled-off flux (i.e., in the second and third phases of the erosion process, see Figure 9), but may miss the completed erosion in which the flux has been completely peeled off.

Based on the orientation obtained from the fittings (see Table 1), we convert the magnetic field components into the magnetic cloud frame. The profiles of  $B_y$  recorded by MESSENGER, VEX, and Wind are shown in Figure 10. Wind spacecraft has valid measurements of solar wind velocity, and therefore the profile of  $v_{x'}$  is plotted in the last panel. Since there is no valid measurements of solar wind velocity in the MESSENGER and VEX data, we simply assume that the magnetic cloud was uniformly propagating through Mercury and Venus. The imbalance of the flux can be evaluated by a revised formula

$$\frac{F_{im}}{v_{x'}L} = \int_{in}^{out} B_y dt \quad (8)$$

The data gaps in the measurements are filled by the linear interpolation. The red curves in Figure 10 are calculated according to equation (8). For the magnetic cloud at the Earth, the data of the recovered uncompressed structure are used. The green curve in the last panel is calculated by equation (7). The red curves in the first two panels are all corrected to the values when the cloud arrives at 1 AU by applying a factor of  $\frac{r}{r_{AU}}$ . In the last panel, the two curves have similar shapes, suggesting that the red curves by equation (8) in the other two panels should be reliable.

It can be seen that an imbalance in the azimuthal magnetic flux can be found at all the three distances and their significances are different. The degree of the imbalance, defined as the ratio of the imbalanced flux to the total flux, is less than 18% at Mercury and the Earth reading from the imbalance curves in the top and bottom panels, and about 75% at Venus. To test the effect of choosing the boundaries on the imbalance, we adjust the boundaries of the cloud by using the same aforementioned method and derive the degree of the imbalance as shown in Figure 11 (also listed in the last column of Table 1). It is found that in our test cases, the degree of the imbalance is small, about 15% at Mercury and then increases to about 77% at Venus and 25% at the Earth. The uncertainty in the imbalance degree at the Earth is quite large, which suggests that the degree might reach up to about 50%. Thus, the erosion effect did exist in this event and probably contributed to the variations of the derived axial flux and twist with the changing heliocentric distance. The difference of the imbalance degree among the three locations might be due to (1) the model errors, (2) the fact that the erosion and peeling-off processes continued to progress between Mercury and the Earth, and/or (3) the fact that some eroded flux has been completely peeled off at some locations and therefore not taken into account by this method. For an ongoing erosion process, magnetic reconnection should happen somewhere at the boundary of the magnetic cloud. As to this event, we do not find any significant signatures of reconnection, implying that the spacecraft probably did not cross the reconnection region.

## 5. Summary and Discussion

In this study, we investigate a magnetic cloud propagating through Mercury, Venus, Earth, and Mars. The magnetic cloud was overtaken by a following fast ejecta and the ejecta-driven shock near the Earth and caused a Forbush decrease at Mars. A method to recover a shock-compressed structure is developed and applied to the magnetic cloud observed by the Wind spacecraft at 1 AU. With the aid of the uniform-twist force-free flux rope model, the axial magnetic flux, helicity, and twist per unit length of the magnetic cloud were derived at three heliocentric distances: Mercury, Venus, and the Earth. It is found that the axial flux and helicity decreased from Mercury to the Earth but the twist increased.

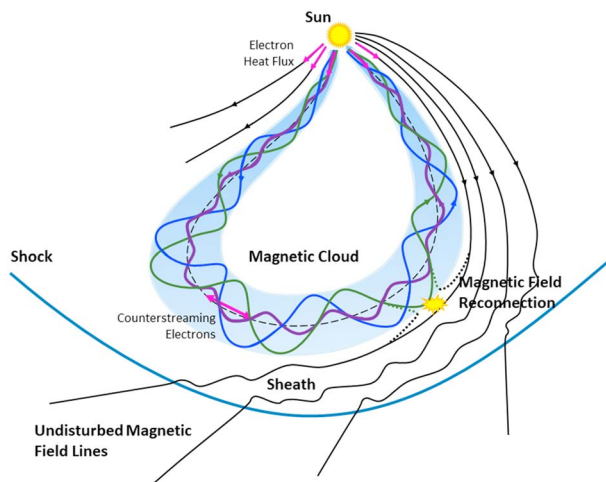


**Figure 12.** A cartoon showing a typical magnetic cloud in the heliosphere, redesigned based on the picture by Zurbuchen and Richardson (2006). The inner purple field line is more twisted than the other two outer lines in the magnetic cloud. The reconnection site implies the erosion process.

Two effects may be responsible for these variations with the heliocentric distance, the pancaking effect and the erosion effect. Our analysis combined with previous simulations and theoretical analysis (e.g., Démoulin & Dasso, 2009; Manchester et al., 2004; Riley et al., 2003; Xiong et al., 2006, 2007) suggests that the pancaking effect may marginally explain the phenomena if the initially cylindrical magnetic cloud was distorted and stretched to a nearly pancake shape with the aspect ratio of its cross section being as large as 3. However, based on the present one-dimensional data, it is difficult to estimate how significant the pancaking effect is for this magnetic cloud. In this scenario, the variations in the axial flux, helicity, and twist do not mean real changes of these properties of the magnetic cloud, but come from the model bias when the shape of the cross section deviates from the cylindrical model.

The erosion effect is evident by the imbalance of the azimuthal magnetic flux at all the three locations: Mercury, Venus, and the Earth. The degree of the imbalance at Mercury, Venus, and the Earth is about 15%, 77%, and 25%, respectively. Although the imbalance degree at Mercury and the Earth is less significant than that at Venus, it does suggest that an erosion process was taking place. This erosion effect may stand alone to explain the variations of the axial flux, helicity, and twist. In this scenario, these vari-

ations are real and imply that the magnetic cloud consists of a high-twist core and a weak-twist outer shell. However, again, we cannot exclude the possibility of the pancaking effect, which more or less happens to magnetic clouds in interplanetary space. Thus, as a conclusion, it is likely that both effects jointly caused such variations with the heliocentric distance.

Since erosion effect exists and the twist increase is real in case of this effect, we would like to discuss its implications on the formation of MFRs. First, the erosion process caused the inner core of the magnetic cloud exposed in the solar wind at far distance. As mentioned before, it leads to the possibility that the twist in the cross section of the initial magnetic cloud was nonuniform, but roughly stage-like distributed with a high-twist core inside. The global picture of an interplanetary magnetic cloud (Zurbuchen & Richardson, 2006) may be further modified as Figure 12, in which the elements of the stage-like twist distribution and an erosion process are incorporated.

Second, back to the debates mentioned at the beginning, if the pancaking effect was insignificant as we argued here, the event presented in this paper supports the scenario that a seed MFR probably exists prior to the CME eruption, and the magnetic field lines added through the magnetic reconnection during the eruption constitute the outer flux with a twist less than the inner seed MFR. Regrettably, the magnetic cloud was a slow and therefore weak one. Its corresponding CME is difficult to be distinguished from other preceding and following CMEs during the period, and its source location is ambiguous (see Appendix B). Thus, we cannot find more supporting material from its source region for this event. But previous studies have showed the possibility of preexisting seed MFRs (e.g., Chintzoglou et al., 2015; Liu, Kliem, et al., 2016), which are thought to be the necessary condition of a successful eruption (Liu, Wang, et al., 2016), based on solar multiple-wavelength observations. The recent theoretical work by Priest and Longcope (2017) also suggested that no high-twist core can form without a preexisting MFR.

Besides, the picture of magnetic field lines possessing a strong twist in the core of a MFR but a weak twist in the outer shell is consistent with the relation of  $\Phi_c = 2 \frac{l}{R}$  (Dungey & Loughhead, 1954; Wang, Zhuang et al., 2016), implying that the outer magnetic field lines twist weaker and weaker when a MFR grows up in terms of the kink instability. Such a stage-like distribution of twist in magnetic clouds was roughly revealed by the Grad-Shafranov reconstruction of magnetic clouds (Hu et al., 2015), and was also showed in the most recent observational work on a solar MFR (Wang et al., 2017). Although the study presented here does not yet reach a definite conclusion about the twist distribution inside the MFR due to the presence of the pancaking effect, we do bring additional insights to the formation and internal structure of MFRs from a unique angle of view. The upcoming space missions “Parker Solar Probe” and “Solar Orbiter” will provide more opportunities for anatomizing an interplanetary magnetic cloud at different distances by multiple radially aligned spacecraft, and the analysis methodology established in this study will show its merits.

### Appendix A: The Corresponding CMEs of Ejecta “E1,” “E3,” and “E4” at Earth and Their Counterparts at Mercury

The ejecta E1, E3, and E4 observed at Earth can be found their counterparts at Mercury. Figure A1 shows the magnetic field during 13–19 February. Except for the magnetic cloud already studied, we can identify other four ejecta, as indicated by light-shadowed regions bounded by vertical blue lines. In all of these regions, the magnetic fields were less fluctuated than ambient magnetic fields and the rotations of field vectors were clear. According the time sequence, we label them as E0 through E4, including the magnetic cloud of interest. Ejecta E3 is much smaller than E1, E2, and E4, but its magnetic field is stronger than theirs. Thus, E3 may continuously expand on its way out to reach a reasonable size at Earth. The arrival times of the front boundaries

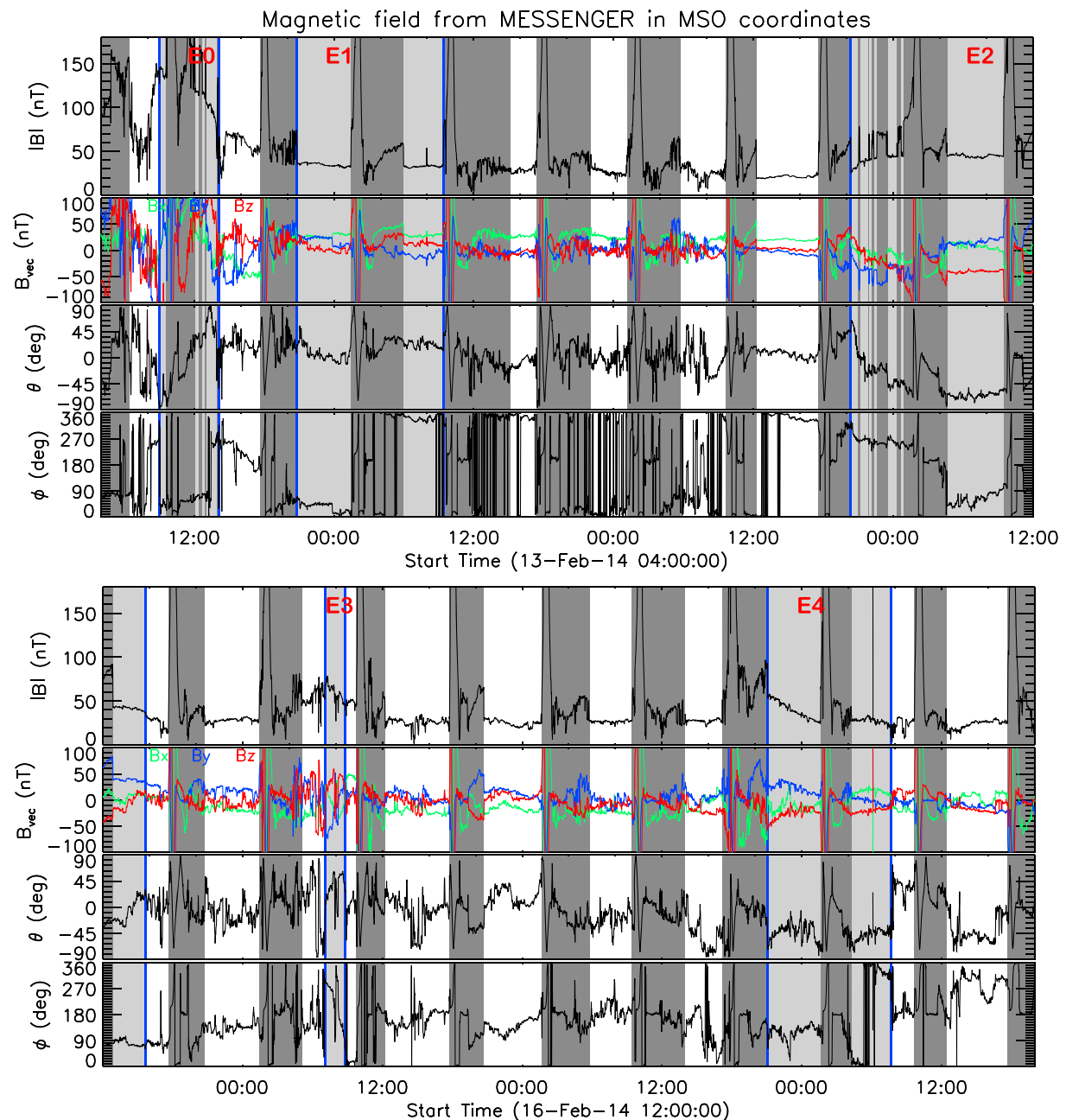


**Figure A1.** Magnetic fields measured by MErcury Surface, Space ENvironment, GEochemistry and Ranging (MESSENGER) from 13 February 04:00 UT to 19 February 20:00 UT. The arrangement is the same as that in Figure 1a. MSO = Mercury solar orbital.

**Table A1***Associations of CMEs in the Corona and Ejecta at Mercury to the Ejecta Observed at Earth*

Ejecta	Earth		Mercury		No.	Corona			GCS			Comment
	$t_e$ (UT)	$v_e$ (km/s)	$t_m$ (UT)	$v_{me}$ (km/s)		$t_c$ (UT)	Width (deg)	Direction	$t_{GCS}$ (UT)	$v_{GCS}$ (km/s)	Direction	
E0	16 04:05	380	13 09:00	400	C0	12 06:00	halo	To Earth	10:20	641	W03°S02°	
						12 13:25	124	To Earth+,N				Out of ecliptic plane
E1	17 19:00	350	13 20:50	290	C1	12 16:36	halo	To Earth+?	20:15?	827?	W31°N09°?	Flank?
						12 23:06	halo	To STA—				Backside
						13 16:36	104	To STA+,S				Backside
						14 08:48	halo	To STA				Backside
E2	18 16:10	400	15 20:20	400	C2	14 11:42	?	?				Stealth?
						14 16:00	145	To STB+,N				Backside
					L1	15 02:24	138	To Earth+	10:35	397	W46°S05°	Limb
						15 09:48	112	To STB,S				Backside
E3	19 13:45	500	17 07:05	490	C3	16 10:00	halo	To Earth	13:20	858	W02°N00°	
						16 12:48	243	To STB+				Backside
E4	21 02:30	500	18 21:05	500	C4	17 03:48	179	To Earth	06:55	857	W04°S08°	
						17 05:12	121	To STA—				Backside
E4*					C5	18 01:36	halo	To Earth—	04:30	1075	E35°S09°	Flank
						18 23:24	133	To STA—,N				Backside

*Note.* The parameters  $t_e$  and  $t_m$  are the arrival times of the ejecta at Earth and Mercury, respectively.  $v_e$  is the in situ speed of the ejecta and  $v_{me}$  is the transit speed of the ejecta from Mercury to Earth.  $t_c$  is the first appearance in the field of view of the Solar and Heliospheric Observatory/Large Angle and Spectroscopic Coronagraph (SOHO/LASCO), and the “Width” is the apparent angular width. The “halo” means the angular width is 360°. The two parameters  $t_c$  and “Width” are adopted from the LASCO coronal mass ejection (CME) catalog Yashiro et al. (2004). The “Direction” under the column “Corona” is estimated by combining the images from the SOHO/LASCO and STEREO/COR2s. “STA” and “STB” stand for the twin STEREO spacecraft A and B. The “plus” sign means that the direction of the CME is west to the Sun-observer line. “S” or “N” means that the CME’s propagation direction is not near the ecliptic plane but toward the high latitude beneath or above the ecliptic plane. The question marks mean that the CME’s parameters are not clear due to contamination by other CMEs. Seven potentially Earth-encountered CMEs are labeled as “C0” through “C5” and “L1” in the column “No.” The columns of “GCS” list the parameters of the CMEs at 20 solar radii obtained by the GCS model, including the time,  $t_{GCS}$ , the real speed,  $v_{GCS}$ , and the propagation direction viewed from Earth. In the last column, “Limb” means that the CME is more than 45° apart from the Sun-Earth line, and “Flank” means that the CME is still able to sweep through the Earth with its flank. The event marked as “E4\*” means that CME “C5” may catch up with the preceding one “C4” and form a complex ejecta as E4 at Earth. GCS = Gradual Cylindrical Shell.

of these ejecta are listed in Table A1. To verify the associations of these ejecta with those at Earth, we calculate their transit speeds,  $v_{me}$ , from Mercury to Earth, which are also listed in Table A1. It is found that the transit speeds of E3 and E4 are well consistent with the in situ speeds of the two ejecta observed at Earth. The association of E1 is also acceptable though its transit speed is about 60 km/s less than its in situ speed. This difference in speed is not too large, considering a possible acceleration due to the interactions of the ejecta with ambient solar wind and also with the following faster ejecta.

Ejecta E0 is right ahead of E1 in the MESSENGER data, which carried a strong magnetic field. This ejecta cannot be associated to E1 at Earth, because the transit speed would be even lower than expected. We check again the data from the Wind spacecraft and find that there was indeed an evident magnetic cloud with an in situ speed of about 380 km/s arriving at Earth at 04:05 UT on 16 February (figure is not shown here, but can be found at our website [http://space.ustc.edu.cn/dreams/wind\\_icmes/](http://space.ustc.edu.cn/dreams/wind_icmes/)), quite consistent with the transit speed of about 400 km/s. In all of these five ejecta observed at Mercury, E2 demonstrates more typical features of a magnetic cloud than others. That is why we choose E2 as the target in this study. It should be noted that only two of the five ejecta, E0 and E3, are listed in the catalog compiled by Winslow et al. (2015) based on the MESSENGER data. We confirm the other three not only based on the features in the magnetic field observed by MESSENGER but also according to the consistent associations between the ejecta at Earth and Mercury. Besides, due to the 20° separation of Venus away from the Sun-Mercury-Earth line, we do not try to make one-to-one associations for these ejecta, which have made the inner heliosphere much disturbed and complicated.



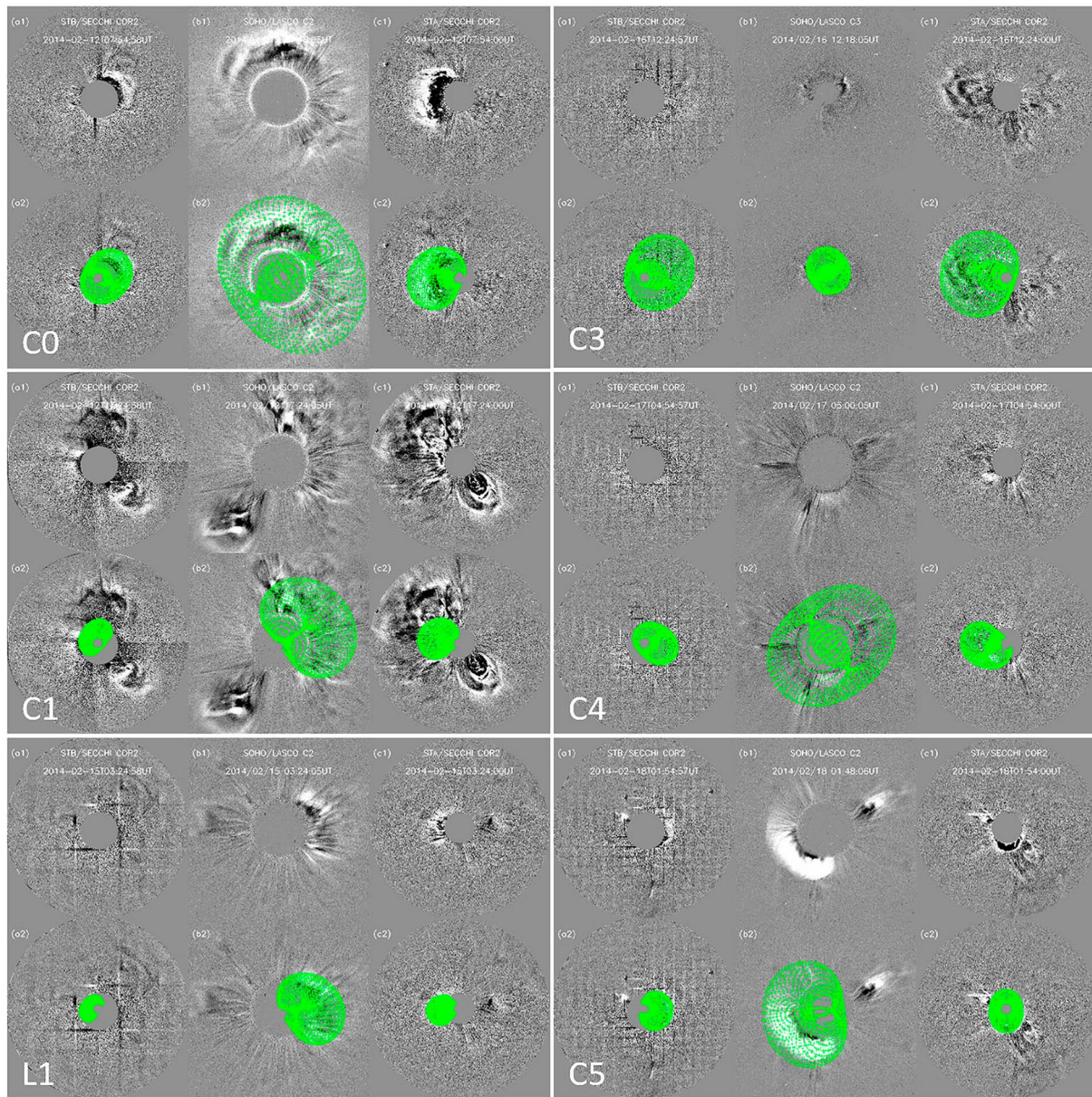


**Figure A2.** Coronagraph images of coronal mass ejections “C0” through “C5” and “L1” (see Table A1), and the same images with GCS fitting meshes (green lines) superimposed on. For each panel, from the left to the right column, it shows the image taken by STEREO-B, SOHO, and STEREO-A, respectively.

The associations of these ejecta with the CMEs observed in coronagraphs are further identified. The Sun was very productive in February of 2014. According to the CME catalog (Yashiro et al., 2004) compiled based on the observations of the Large Angle and Spectroscopic CORonagraph (LASCO, Brueckner et al., 1995) on board the Solar and Heliospheric Observatory (SOHO) and our own manually checked with the coronagraph images from COR2s of the SECCHI packages (Howard et al., 2008) on board the STEREO-A and B and the images from SOHO/LASCO, there were 16 CMEs with apparent angular width larger than  $90^\circ$  as listed in Table A1. Not all of them directed to Earth. By combining the images from SOHO/LASCO and STEREO-A and B/COR2s, we can roughly determine the propagation directions of these CMEs. The position of the three spacecraft can be found in Figure 3. It is found that only CMEs labeled as “C0” through “C5” and “L1” are candidates. “C2” is not listed in the LASCO CME catalog, and we think it is the most probable candidate of the magnetic cloud of interest in this study, which will be discussed in the next section. Here we focus on the rest. To get more accurate kinematic parameters of these CMEs in three-dimensional space, we apply a forward modeling



to the coronagraph images with the aid of Gradual Cylindrical Shell (GCS) model (Thernisien, 2011). The modeled parameters, which correspond to the CME's leading edge at 20 solar radii, are listed in Table A1. The meshes fitting to the outlines of these CMEs are shown in Figure A2.

CMEs C0, C3–C5, and L1 can be well recognized in the coronagraphs on board the SOHO and STEREO-A and B, and therefore can be well fitted. In these CMEs, L1 is a limb event viewed from Earth. Its speed was close to the ambient solar wind, and therefore, no significant deflection is expected (Wang, Zhang, et al., 2016). Thus, this CME should not be able to encounter Mercury and Earth. The other CMEs C0, C3–C5 are thought to be responsible for ejecta E0, E3, and E4. CME C5 was particularly fast. Though it propagated west to the Sun-Earth line in the corona, it may be deflected toward the Sun-Earth line in interplanetary space according to our DIPS model (Wang, Zhang, et al., 2016). Thus, it was able to catch up with the preceding one C4 and formed a complex ejecta at Earth. It is noteworthy that all of these CMEs had a faster speed than the transit speed from Mercury to Earth. This phenomenon is reasonable as CMEs will be quickly assimilated to the ambient solar wind in terms of speed (Gopalswamy et al., 2000). The GCS fitting of CME C1, however, is not confident, because the CME followed another one, which made it very blurry, especially in the field of view of the STEREO-B/COR2. Based on the current GCS fitting, the CME initially propagated along the direction 30° away from Earth and might be deflected toward the Sun-Earth line in interplanetary space to encounter Mercury and Earth with its flank.

### Appendix B: Identify the Corresponding CME and Source Region of the Magnetic Cloud of Interest “E2”

According to the above DIPS model result, the magnetic cloud speed is about 400 km/s, and the expected onset time of the corresponding CME is at about 09:00 UT on 14 February. We check all the CMEs with apparent angular width larger than 90° during 13–15 February, which can be found in Table A1. There are six CMEs for consideration, among which four CMEs were almost backside as identified in the previous subsection. CME L1 was a limb event and too slow to be the corresponding CME of the magnetic cloud. CME C2 is not in the LASCO CME catalog. By manually checking the coronagraphs images, we find there was a weak CME entering the field of view of SOHO LASCO at about 11:42 UT on 14 February, right behind the strong CME appearing on 08:48 UT. Two snapshots taken by SOHO/LASCO C2 and STEREO-B/COR2 cameras, respectively, are shown in Figure B1. We do not show the images from STEREO-A, because the quality is not good enough. In the left panel, there were three CME-like structures, one toward the southwest in the plane of the sky and the other two, very close to each other, toward the northeast. The upper one in the northeast direction can be identified as a high-latitude CME toward the east of the Sun-Earth line from the SOHO/LASCO and STEREO-A and B's

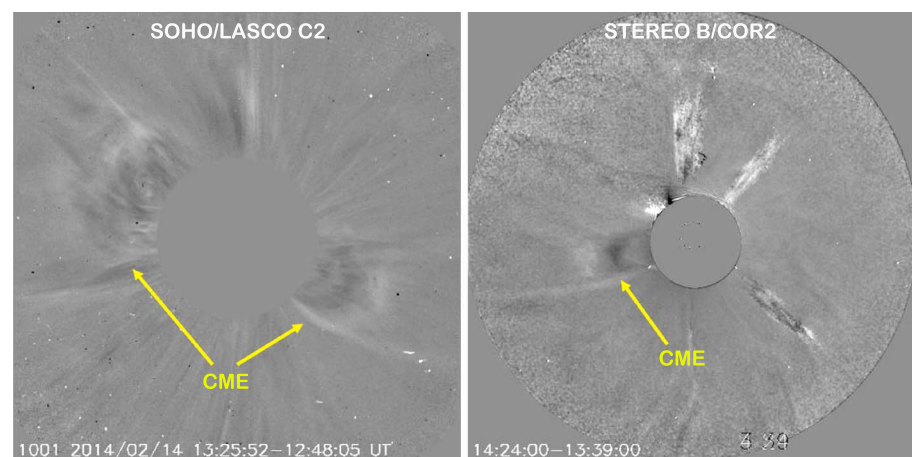


**Figure B1.** Most possible coronal mass ejection (CME) candidate for the magnetic cloud in the coronagraphs. (a) The difference image taken by the Solar and Heliospheric Observatory/Large Angle and Spectroscopic COroNagraph C2 camera. (b) The difference image taken by the STEREO-B/COR2 camera. The candidate CME structures are denoted by the arrows.

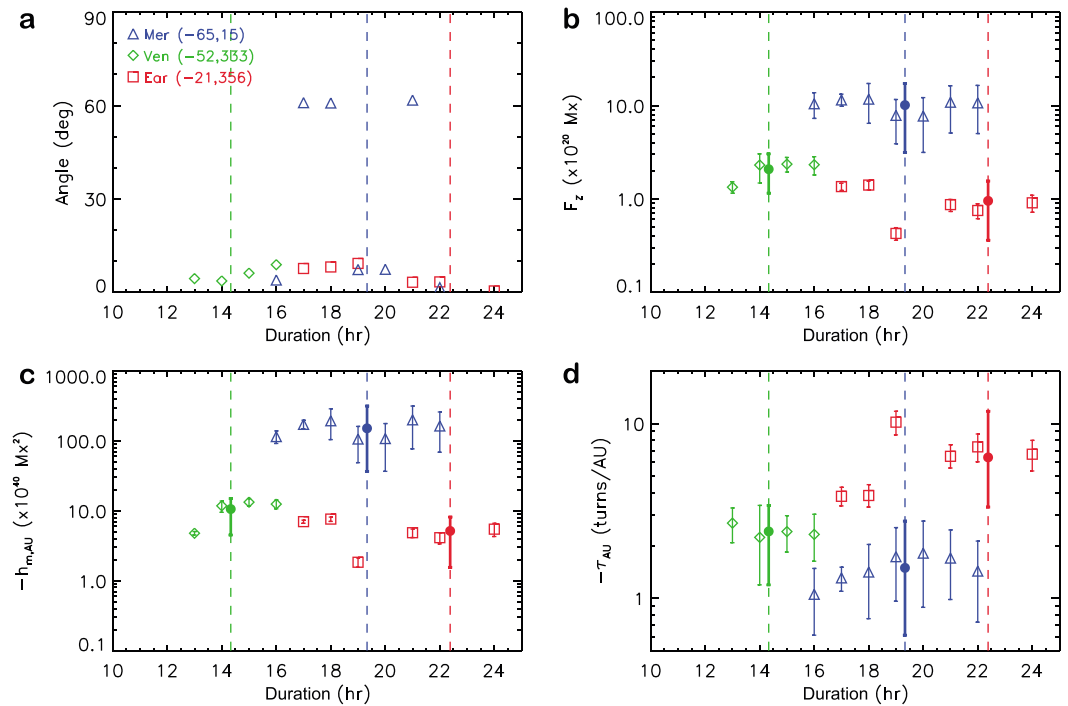


**Figure C1.** Same as Figure 5 except that we set an expansion speed to be 20 km/s when fitting the magnetic cloud at Mercury.

COR2 images (not shown here). However, it is not clear whether or not the lower one belonged to the same CME of the southwest one. If it was true, the CME right faced on Earth as expected. However, in the right panel of the figure, we can only recognize one CME structure toward the east from the view of STEREO-B, which corresponds to the southwest structure in the SOHO/LASCO image. This makes the identification ambiguous.

Even if the southwest CME was the most probable candidate, the EUV images taken by the Atmospheric Imaging Assembly (Lemen et al., 2012) on board the Solar Dynamics Observatory (SDO) show no signature of the CME on the solar surface in a reasonable period before the CME appeared in the field of view of the SOHO/LASCO. Thus, it is also possible that the magnetic cloud observed by MESSENGER corresponds to a stealth CME (e.g., Howard & Harrison, 2013; Ma et al., 2010; Robbrecht et al., 2009; Wang et al., 2011).

### Appendix C: Influence of the Nonexpansion Assumption on the Fitting Results

The Wind data suggest that the magnetic cloud might experience a weak expansion with a speed of about 20 km/s at 1 AU (see  $v_x$  profile in Figure 6). However, in our fitting procedure for the magnetic cloud at Mercury and Venus, the expansion speed is assumed to be zero, which might influence the fitting results. To test how significant the influence will be, we set the expansion speed to be 20 km/s for the cloud at Mercury and run the fitting code again. The test results are shown in Figures C1 and C2, which correspond to Figures 5 and 11 in the main text, respectively. By comparing the blue symbols in the two sets of figures, it could be found that there is no evident difference in the axial flux, magnetic helicity, twist, and the degree of imbalance, except for two more test cases with orientations deviating largely from the final orientation determined for nonexpansion cases. The comparison suggests that the assumption of nonexpansion speed has small influence on our results and conclusions.

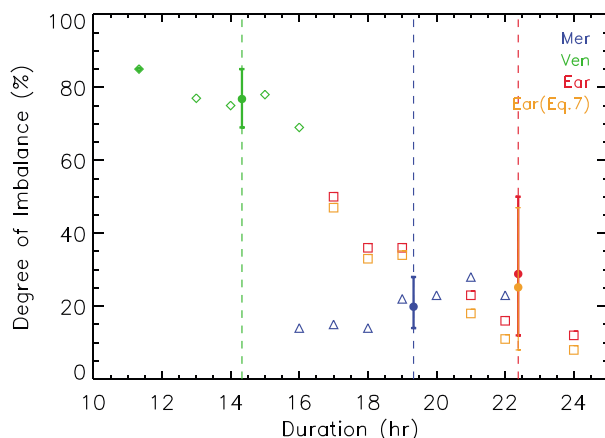


**Figure C2.** Same as Figure 1 except that we set an expansion speed to be 20 km/s when fitting the magnetic cloud at Mercury.

## Acknowledgments

We acknowledge the use of the data from the magnetometers on board the MESSENGER, VEX, and Wind spacecraft, the Solar Wind Experiment (SWE) on board Wind spacecraft, the RAD on board the MSL, and EUV imagers and coronagraphs on board the Solar Dynamics Observatory (SDO), Solar and Heliospheric Observatory (SOHO), and the twin Solar Terrestrial Relations Observatories (STEREO). We do appreciate the constructive comments from anonymous referees, which make the paper much better. Y. W. is grateful to the valuable discussion with Hui Li from Los Alamos National Laboratory about the astrophysical jets and high-twist phenomena. J. G. acknowledges stimulating discussions with the ISSI team "Radiation Interactions at Planetary Bodies" and thanks ISSI for its hospitality. Y. W. acknowledges the support from NSFC grants 41774178 and 41574165, R. L. the support from NSFC grants 41474151 and 41774150 and the Thousand Young Talents Program of China, J. L. the support from the Science and Technology Facility Council (STFC) of UK, and Q. H. partial support from NASA grant NNX14AF41G and NRL contract N00173-14-1-G006. This work is also supported by NSFC grants 41761134088 and 41421063 and the fundamental research funds for the central universities.

## References

- Anderson, B. J., Acuña, M. H., Lohr, D. A., Scheifele, J., Raval, A., Korth, H., et al. (2007). The magnetometer instrument on MESSENGER. *Space Science Reviews*, 131, 417–450.
- Antiochos, S. K., DeVore, C. R., & Klimchuk, J. A. (1999). A model for solar coronal mass ejections. *The Astrophysical Journal*, 510, 485–493.
- Aulanier, G., Janvier, M., & Schmieder, B. (2012). The standard flare model in three dimensions I. Strong-to-weak shear transition in post-flare loops. *Astronomy & Astrophysics*, 543(A110), 14.
- Aulanier, G., Török, T., Démoulin, P., & DeLuca, E. E. (2010). Formation of torus-unstable flux ropes and electric currents in erupting sigmoids. *The Astrophysical Journal*, 708, 314–333.
- Brueckner, G. E., Howard, R. A., Koomen, M. J., Korendyke, C. M., Michels, D. J., Moses, J. D., et al. (1995). The large angle spectroscopic coronagraph (LASCO). *Solar Physics*, 162, 357–402.
- Burlaga, L., Sittler, E., Mariani, F., & Schwenn, R. (1981). Magnetic loop behind an interplanetary shock: Voyager, Helios, and IMP 8 observations. *Journal of Geophysical Research*, 86, 6673–6684.
- Cane, H. V. (2000). Coronal mass ejections and forrush decreases. *Space Science Reviews*, 93, 55–77.
- Chintzoglou, G., Patsourakos, S., & Vourlidas, A. (2015). Formation of magnetic flux ropes during confined flaring well before the onset of a pair of major coronal mass ejections. *The Astrophysical Journal*, 809(34), 18.
- Cid, C., Hidalgo, M. A., Nieves-Chinchilla, T., Sequeiros, J., & Viñas, A. F. (2002). Plasma and magnetic field inside magnetic clouds: A global study. *Solar Physics*, 207, 187–198.
- Crooker, N. V., & Intriligator, D. S. (1996). A magnetic cloud as a distended flux rope occlusion in the heliospheric current sheet. *Journal of Geophysical Research*, 101, 24,343–24,348.
- Dasso, S., Mandrini, C. H., Démoulin, P., & Luoni, M. L. (2006). A new model-independent method to compute magnetic helicity in magnetic clouds. *Astronomy & Astrophysics*, 455, 349–359.
- Daughton, W., Roytershteyn, V., Karimabadi, H., Yin, L., Albright, B. J., Bergen, B., et al. (2011). Role of electron physics in the development of turbulent magnetic reconnection in collisionless plasmas. *Nature Physics*, 7, 539–542.
- Démoulin, P., & Dasso, S. (2009). Causes and consequences of magnetic cloud expansion. *Astronomy & Astrophysics*, 498, 551–566.
- Du, D., Wang, C., & Hu, Q. (2007). Propagation and evolution of a magnetic cloud from ACE to Ulysses. *Journal of Geophysical Research*, 112, A09101. <https://doi.org/10.1029/2007JA012482>
- Dungey, J. W., & Loughhead, R. E. (1954). Twisted magnetic fields in conducting fluids. *Australian Journal of Physics*, 7, 5–13.
- Gary, G. A., & Moore, R. L. (2004). Eruption of a multi-turn helical magnetic flux tube in a large flare: Evidence for external and internal reconnection that fits the breakout model of solar magnetic eruptions. *The Astrophysical Journal*, 611, 545–556.
- Goldstein, H. (1983). On the field configuration in magnetic clouds. In *Solar wind five* (Vol. 731, pp. 2280). Washington DC: NASA Conf. Publ.
- Gómez, J. L., Marscher, A. P., Jorstad, S. G., Agudo, I., & Roca-Sogorb, M. (2008). Faraday rotation and polarization gradients in the jet of 3C 120: Interaction with the external medium and a helical magnetic field? *The Astrophysical Journal*, 681, L69–L72.
- Good, S., Forsyth, R., Raines, J. M., Gershman, D. J., Slavin, J. A., & Zurbuchen, T. H. (2015). Radial evolution of a magnetic cloud: MESSENGER, STEREO, and Venus Express observations. *The Astrophysical Journal*, 807(177), 12.
- Gopalswamy, N., Lara, A., Lepping, R. P., Kaiser, M. L., Berdichevsky, D., & St. Cyr, O. C. (2000). Interplanetary acceleration of coronal mass ejections. *Geophysical Research Letters*, 27, 145–148.
- Gosling, J. T. (2012). Magnetic reconnection in the solar wind. *Space Science Reviews*, 172, 187–200.
- Grotzinger, J. P., Crisp, J., Vasavada, A. R., Anderson, R. C., Baker, C. J., Barry, R., et al. (2012). Mars science laboratory mission and science investigation. *Space Science Reviews*, 170, 5–56.
- Guo, J., Lillis, R., Wimmer-Schweingruber, R. F., Zeitlin, C., Simonson, P., Rahmati, A., et al. (2018). Measurements of Forbush decreases at Mars: Both by MSL on ground and by MAVEN in orbit. *Astronomy & Astrophysics*, 611, A79. <https://doi.org/10.1051/0004-6361/201732087>
- Guo, J., Slaba, T. C., Zeitlin, C., Wimmer-Schweingruber, R. F., Badavi, F. F., Böhm, E., et al. (2017). Dependence of the Martian radiation environment on atmospheric depth: Modeling and measurement. *Journal of Geophysical Research: Planets*, 122, 329–341. <https://doi.org/10.1002/2016JE005206>
- Hassler, D. M., Zeitlin, C., Wimmer-Schweingruber, R. F., Böttcher, S., Martin, C., Andrews, J., et al. (2012). The radiation assessment detector (RAD) investigation. *Space Science Reviews*, 170, 503–558.
- Hidalgo, M. A., Cid, C., Vinas, A. F., & Sequeiros, J. (2002). A non-force-free approach to the topology of magnetic clouds in the solar wind. *Journal of Geophysical Research*, 107(01), 1002. <https://doi.org/10.1029/2001JA000100>
- Hood, A. W., & Priest, E. R. (1981). Critical conditions for magnetic instabilities in force-free coronal loops. *Geophysical and Astrophysical Fluid Dynamics*, 17, 297–318.
- Howard, R. A., Moses, J., Vourlidas, A., Newmark, J. S., Socker, D. G., Plunkett, S. P., et al. (2008). Sun earth connection coronal and heliospheric investigation (SECCHI). *Space Science Reviews*, 136, 67–115.
- Howard, T. A., & Harrison, R. A. (2013). Stealth coronal mass ejections: A perspective. *Solar Physics*, 285, 269–280.
- Hu, Q., & Sonnerup, B. U. O. (2002). Reconstruction of magnetic clouds in the solar wind: Orientations and configurations. *Journal of Geophysical Research*, 107(07), 1142. <https://doi.org/10.1029/2001JA000293>
- Hu, Q., Qiu, J., & Krucker, S. (2015). Magnetic field line lengths inside interplanetary magnetic flux ropes. *Journal of Geophysical Research: Space Physics*, 120, 5266–5283. <https://doi.org/10.1002/2015JA021133>
- Karpen, J. T., Antiochos, S. K., & DeVore, C. R. (2012). The mechanisms for the onset and explosive eruption of coronal mass ejections and eruptive flares. *The Astrophysical Journal*, 760, 81.
- Kopp, R. A., & Pneuman, G. W. (1976). Magnetic reconnection in the corona and the loop prominence phenomenon. *Solar Physics*, 50, 85–98.
- Kruskal, M. D., Johnson, J. L., Gottlieb, M. B., & Goldman, L. M. (1958). Hydromagnetic instability in a stellarator. *Physics of Fluids*, 1, 421–429.
- Leitner, M., Farrugia, C. J., Mo'stl, C., Ogilvie, K. W., Galvin, A. B., Schwenn, R., et al. (2007). Consequences of the force-free model of magnetic clouds for their heliospheric evolution. *Journal of Geophysical Research*, 112, A06113. <https://doi.org/10.1029/2006JA011940>
- Lemen, J. R., Title, A. M., Akin, D. J., Boerner, P. F., Chou, C., Drake, J. F., et al. (2012). The atmospheric imaging assembly (AIA) on the solar dynamics observatory (SDO). *Solar Physics*, 275, 17–40.
- Lepping, R. P., Acuna, M. H., Burlaga, L. F., Farrell, W. M., Slavin, J. A., Schatten, K. H., et al. (1995). The Wind magnetic field investigation. *Space Science Reviews*, 71, 207–229.
- Lepping, R. P., Berdichevsky, D. B., Wu, C.-C., Szabo, A., Narock, T., Mariani, F., et al. (2006). A summary of WIND magnetic clouds for years 1995–2003: Model-fitted parameters, associated errors and classifications. *Annales de Geophysique*, 24, 215–245.
- Lepping, R. P., Jones, J. A., & Burlaga, L. F. (1990). Magnetic field structure of interplanetary magnetic clouds at 1 AU. *Journal of Geophysical Research*, 95, 11,957–11,965.
- Liu, L., Wang, Y., Wang, J., Shen, C., Ye, P., Liu, R., et al. (2016). Why is a flare-rich active region CME-poor? *The Astrophysical Journal*, 826(119), 10.

- Liu, R., Kliem, B., Titov, V. S., Chen, J., Wang, Y., Wang, H., et al. (2016). Structure, stability, and evolution of magnetic flux ropes from the perspective of magnetic twist. *The Astrophysical Journal*, 818(148), 22.
- Longcope, D. W., & Beveridge, C. (2007). A quantitative, topological model of reconnection and flux rope formation in a two-ribbon flare. *The Astrophysical Journal*, 669, 621–635.
- Lundquist, S. (1950). Magnetohydrostatic fields. *Arkiv för Fysik*, 2, 361.
- Ma, S., Attrill, G. D. R., Golub, L., & Lin, J. (2010). Statistical study of coronal mass ejections with and without distinct low coronal signatures. *The Astrophysical Journal*, 722, 289–301.
- Manchester, W. B., Gombosi, T. I., Roussev, I., De Zeeuw, D. L., Sokolov, I. V., Powell, K. G., et al. (2004). Three-dimensional MHD simulation of a flux rope driven CME. *Journal of Geophysical Research*, 109, A01102. <https://doi.org/10.1029/2002JA009672>
- Manchester, W. B., Kozyra, J. U., Lepri, S. T., & Lavraud, B. (2014). Simulation of magnetic cloud erosion during propagation. *Journal of Geophysical Research: Space Physics*, 119, 5449–5464. <https://doi.org/10.1002/2014JA019882>
- Marscher, A. P., Jorstad, S. G., D'Arcangelo, F. D., Smith, P. S., Grant Williams, G., Larionov, V. M., et al. (2008). The inner jet of an active galactic nucleus as revealed by a radio-to- $\gamma$ -ray outburst. *Nature*, 452, 966–969.
- Marubashi, K. (1986). Structure of the interplanetary magnetic clouds and their solar origins. *Advances in Space Research*, 6, 335–338.
- Moore, R. L., Sterling, A. C., Hudson, H. S., & Lemen, J. R. (2001). Onset of the magnetic explosion in solar flares and coronal mass ejections. *The Astrophysical Journal*, 552, 833–848.
- Möstl, C., & Davies, J. A. (2013). Speeds and arrival times of solar transients approximated by self-similar expanding circular fronts. *Solar Physics*, 285, 411–423.
- Mulligan, T., & Russell, C. T. (2001). Multispacecraft modeling of the flux rope structure of interplanetary coronal mass ejections: Cylindrically symmetric versus nonsymmetric topologies. *Journal of Geophysical Research*, 106(A6), 10,581–10,596.
- Mulligan, T., Russell, C. T., Anderson, B. J., & Acuna, M. H. (2001). Multiple spacecraft flux rope modeling of the Bastille Day magnetic cloud. *Geophysical Research Letters*, 28(23), 4417–4420.
- Myers, C. E., Yamada, M., Ji, H., Yoo, J., Fox, W., Jara-Almonte, J., et al. (2015). A dynamic magnetic tension force as the cause of failed solar eruptions. *Nature*, 528, 526–529.
- Nakwacki, M. S., Dasso, S., Démoulin, P., Mandrini, C. H., & Gulisano, A. M. (2011). Dynamical evolution of a magnetic cloud from the Sun to 5.4 AU. *Astronomy & Astrophysics*, 535, A52.
- Nieves-Chinchilla, T., Colaninno, R., Vourlidas, A., Szabo, A., Lepping, R. P., Boardsen, S. A., et al. (2012). Remote and in situ observations of an unusual Earth-directed coronal mass ejection from multiple viewpoints. *Journal of Geophysical Research*, 117, A06106. <https://doi.org/10.1029/2011JA017243>
- Ogilvie, K. W., Chornay, D. J., Fritzenreiter, R. J., Hunsaker, F., Keller, J., Lobell, J., et al. (1995). SWE, a comprehensive plasma instrument for the Wind spacecraft. *Space Science Reviews*, 71, 55–77.
- Owen, F. N., Hardee, P. E., & Cornwell, T. J. (1989). High-resolution, high dynamic range VLA images of the M87 jet at 2 centimeters. *The Astrophysical Journal*, 340, 698–707.
- Perley, R. A., Bridle, A. H., & Willis, A. G. (1984). High-resolution VLA observations of the radio jet in NGC 6251. *The Astrophysical Journal*, 54, 291–334.
- Priest, E. R., & Longcope, D. W. (2017). Flux-rope twist in eruptive flares and CMEs: Due to zipper and main-phase reconnection. *Solar Physics*, 292, 25.
- Qiu, J., Hu, Q., Howard, T. A., & Yurchyshyn, V. B. (2007). On the magnetic flux budget in low-corona magnetic reconnection and interplanetary coronal mass ejections. *The Astrophysical Journal*, 659, 758–772.
- Riley, P., & Crooker, N. U. (2004). Kinematic treatment of coronal mass ejection evolution in the solar wind. *The Astrophysical Journal*, 600, 1035–1042.
- Riley, P., Linker, J. A., Lionello, R., Mikic, Z., Odstrcil, D., Hidalgo, M. A., et al. (2004). Fitting flux ropes to a global MHD solution: A comparison of techniques. *Journal of Atmospheric and Solar-Terrestrial Physics*, 66, 1321–1331.
- Riley, P., Linker, J. A., Mikic, Z., Odstrcil, D., Zurbuchen, T. H., Lario, R. P., et al. (2003). Using an MHD simulation to interpret the global context of a coronal mass ejection observed by two spacecraft. *Journal of Geophysical Research*, 108(A7), 1272. <https://doi.org/10.1029/2002JA009760>
- Robbrecht, E., Patsourakos, S., & Vourlidas, A. (2009). No trace left behind: STEREO observation of a coronal mass ejection without low coronal signatures. *The Astrophysical Journal*, 701, 283–291.
- Ruffenach, A., Lavraud, B., Farrugia, C. J., Démoulin, P., Dasso, S., Owens, M. J., et al. (2015). Statistical study of magnetic cloud erosion by magnetic reconnection. *Journal of Geophysical Research: Space Physics*, 120, 43–60. <https://doi.org/10.1002/2014JA020628>
- Ruffenach, A., Lavraud, B., Owens, M. J., Sauvaud, J.-A., Savani, N. P., Rouillard, A. P., et al. (2012). Multispacecraft observation of magnetic cloud erosion by magnetic reconnection during propagation. *Journal of Geophysical Research*, 117, A09101. <https://doi.org/10.1029/2012JA017624>
- Russell, C. T., & Mulligan, T. (2002). The true dimensions of interplanetary coronal mass ejections. *Advances in Space Research*, 29, 301–306.
- Shafranov, V. D. (1963). Equilibrium of a toroidal plasma in a magnetic field. *Journal of Nuclear Energy*, 5, 251–258.
- Shen, C., Wang, Y., Pan, Z., Miao, B., Ye, P., & Wang, S. (2014). Full-halo coronal mass ejections: Arrival at the Earth. *Journal of Geophysical Research: Space Physics*, 119, 5107–5116. <https://doi.org/10.1002/2014JA020001>
- Slavin, J. A. (2004). Mercury's magnetosphere. *Advances in Space Research*, 33, 1859–1874.
- Srivastava, A. K., Zaqarashvili, T. V., Kumar, P., & Khodachenko, M. L. (2010). Observation of kink instability during small B5.0 solar flare on 2007 June 4. *The Astrophysical Journal*, 715, 292–299.
- Svedhem, H., Titov, D. V., McCoy, D., Lebreton, J.-P., Barabash, S., Bertaux, J.-L., et al. (2007). Venus Express—The first European mission to Venus. *Planetary and Space Science*, 55, 1636–1652.
- Szabo, A. (1994). An improved solution to the 'Rankine-Hugoniot' problem. *Journal of Geophysical Research*, 99, 14,737–14,746.
- Thernisien, A. (2011). Implementation of the graduated cylindrical shell model for the three-dimensional reconstruction of coronal mass ejections. *The Astrophysical Journal Supplement*, 194, 33.
- Titov, V. S., & Démoulin, P. (1999). Basic topology of twisted magnetic configurations in solar flares. *Astronomy & Astrophysics*, 351, 707–720.
- van Ballegoijen, A. A., & Martens, P. C. H. (1989). Formation and eruption of solar prominences. *The Astrophysical Journal*, 343, 971–984.
- Vandas, M., & Romashets, E. P. (2003). A force-free field with constant alpha in an oblate cylinder: A generalization of the Lundquist solution. *Astronomy & Astrophysics*, 398, 801–807.
- Viñas, A. F., & Scudder, J. D. (1984). Fast and optimal solution to the 'Rankine-Hugoniot problem'. *Journal of Geophysical Research*, 91, 39–58.
- Vourlidas, A., Lynch, B. J., Howard, R. A., & Li, Y. (2013). How many CMEs have flux ropes? Deciphering the signatures of shocks, flux ropes, and prominences in coronagraph observations of CMEs. *Solar Physics*, 284, 179–201.
- Vršnak, B., Ruzdjak, V., & Rimpolt, B. (1991). Stability of prominences exposing helical-like patterns. *Solar Physics*, 136, 151–167.

- Wang, W., Liu, R., Wang, Y., Hu, Q., Shen, C., Jiang, C., et al. (2017). Buildup of a highly twisted magnetic flux rope during a solar eruption. *Nature Communications*, 8, 1330.
- Wang, Y., Chen, C., Gui, B., Shen, C., Ye, P., & Wang, S. (2011). Statistical study of coronal mass ejection source locations: Understanding cmes viewed in coronagraphs. *Journal of Geophysical Research*, 116, A04104. <https://doi.org/10.1029/2010JA016101>
- Wang, Y., Shen, C., Ye, P., & Wang, S. (2004). Deflection of coronal mass ejection in the interplanetary medium. *Solar Physics*, 222, 329–343.
- Wang, Y., Zhang, Q., Liu, J., Shen, C., Shen, F., Yang, Z., et al. (2016). On the propagation of a geoeffective coronal mass ejection during 15–17 March 2015. *Journal of Geophysical Research: Space Physics*, 121, 7423–7434. <https://doi.org/10.1002/2016JA022924>
- Wang, Y., Zhou, Z., Shen, C., Liu, R., & Wang, S. (2015). Investigating plasma motion of magnetic clouds at 1 AU through a velocity-modified cylindrical force-free flux rope model. *Journal of Geophysical Research: Space Physics*, 120, 1543–1565. <https://doi.org/10.1002/2014JA020494>
- Wang, Y., Zhuang, B., Hu, Q., Liu, R., Shen, C., & Chi, Y. (2016). On the twists of interplanetary magnetic flux ropes observed at 1 AU. *Journal of Geophysical Research: Space Physics*, 121, 9316–9339. <https://doi.org/10.1002/2016JA023075>
- Winslow, R. M., Lugaz, N., Philpott, L. C., Schwadron, N. A., Farrugia, C. J., Anderson, B. J., et al. (2015). Interplanetary coronal mass ejections from MESSENGER orbital observations at Mercury. *Journal of Geophysical Research: Space Physics*, 120, 6101–6118. <https://doi.org/10.1002/2015JA021200>
- Winslow, R. M., Lugaz, N., Schwadron, N. A., Farrugia, C. J., Yu, W., Raines, J. M., et al. (2016). Longitudinal conjunction between MESSENGER and STEREO A: Development of ICME complexity through stream interactions. *Journal of Geophysical Research: Space Physics*, 121, 6092–6106. <https://doi.org/10.1002/2015JA022307>
- Xiong, M., Zheng, H., Wang, Y., & Wang, S. (2006). Magnetohydrodynamic simulation of the interaction between interplanetary strong shock and magnetic cloud and its consequent geoeffectiveness. *Journal of Geophysical Research*, 111, A08105.
- Xiong, M., Zheng, H., Wu, S. T., Wang, Y., & Wang, S. (2007). Magnetohydrodynamic simulation of the interaction between two interplanetary magnetic clouds and its consequent geoeffectiveness. *Journal of Geophysical Research*, 112, A11103. <https://doi.org/10.1029/2007JA012320>
- Yashiro, S., Gopalswamy, N., Michalek, G., Cyr, O. C. S. t., Plunkett, S. P., Rich, N. B., et al. (2004). A catalog of white light coronal mass ejections observed by the SOHO spacecraft. *Journal of Geophysical Research*, 109, A07105. <https://doi.org/10.1029/2003JA010282>
- Zhang, J., Cheng, X., & Ding, M.-D. (2012). Observation of an evolving magnetic flux rope before and during a solar eruption. *Nature Communications*, 3, 747.
- Zhang, T. L., Baumjohann, W., Delva, M., Auster, H.-U., Balogh, A., Russell, C. T., et al. (2006). Magnetic field investigation of the Venus plasma environment: Expected new results from Venus Express. *Planetary and Space Science*, 54, 13–14.
- Zhuang, B., Wang, Y., Shen, C., Liu, S., Wang, J., Pan, Z., et al. (2017). Significance of the influence of the CME deflection in interplanetary space on the CME arrival at the Earth. *The Astrophysical Journal*, 845(117), 12.
- Zurbuchen, T. H., & Richardson, I. G. (2006). In-situ solar wind and magnetic field signatures of interplanetary coronal mass ejections. *Space Science Reviews*, 123, 31–43.